



INTERNSHIP (SEMESTER THESIS) REPORT

Development of a Dual-Spectral Imaging System for Flame Thermography in a Model Rocket Engine

Author: Yasir, Muhammad

Supervisros: Winter, Fernanda, M.Sc.
Perakis, Nikolaos, M.Sc.

Dated: 15.02.2019

DOI: 10.14459/2022md1658212



Declaration of Authorship

I hereby declare that this thesis is my own work prepared without the help of a third party. No other than the listed literature and resources have been used. All sources transferred literally or analogously to this work have been labeled accordingly.

Additionally, I hereby certify that this thesis has not been underlain in any other examination procedure up to the present.

Muhammad Yasir

.....
Signature



Abstract

A simple optical system for measurement of 2D temperature field was developed for a model rocket engine available at the chair of Turbomachinery & Flight Propulsion of Technical University of Munich. The rocket engine was provided with an optical access on one side of the combustor. A band ratio technique (similar to the two-colour method) was employed in which integrated intensities in two spectral bands were imaged using a CMOS greyscale camera. The two bands selected were centred at 850 nm and 925 nm with a width (FWHM) of 25 nm each. The temperature was calibrated against the intensity ratio of two bands using methane-air and methane-oxygen flames on a flat flame (McKenna) burner. Soot was not significant even in rich flames and the same calibration curve was found to be valid for both the fuel-oxidiser combinations for lean, rich, and stoichiometric conditions. Two methods were investigated for determination of temperatures. In method-1, the calibration was performed using temperatures known from DLR experiments for standard methane-air flames. This calibration was used to calculate temperatures for methane-oxygen flames which were validated against reference temperatures known from previous study. In method-2, an alumina-silica fibre (~36 μm diameter) was used as a thin filament pyrometer (TFP) to measure temperatures in methane-oxygen flames which were then used for calibration. Calculations of temperature field were done using this calibration for methane-air and methane-oxygen flames which were validated against reference values from previous studies. In both the methods, the error in temperatures was higher close to the burner and decreased with height. This was due to camera misalignment and uncertainty in reference temperatures close to the burner surface. Focusing on a region from 5 mm to 15 mm above the burner exit, the error in method-1 was within 10% and for method-2 it was within 13%. No direct control on flowrates was available and they were indirectly set using pressure regulators of limited precision. This was the main source of error in both methods. Further to this contributor, multifilament nature of the fibre resulting in inhomogeneity contributed to error in TFP measurements and hence in method-2. The maximum error in TFP measurements was found to be ~12%. Application of the measurement setup to the rocket engine was assessed. It is shown that the same calibration curve can be applied to the rocket engine flame. Pointers for further investigation and improvements are also given.



Contents

List of Figures	III
List of Tables	V
List of Symbols	VI
List of Abbreviations	VII
1 Introduction	1
1.1 Importance of Flame Temperature Determination	1
1.2 Project Objective & Scope	1
2 Literature Review	2
2.1 Probe Methods.....	2
2.1.1 Fine Wire Thermocouple	2
2.1.2 Thin Filament Pyrometer (TFP).....	3
2.2 Optical Methods	4
2.2.1 Disappearing Filament Pyrometer	4
2.2.2 Absolute Camera Calibration.....	5
2.2.3 Flame Emissivity Determination using Background Radiation.....	5
2.2.4 CO ₂ Based Spectral Infrared Thermography	6
2.2.5 Two-Colour Method.....	7
2.2.6 Band Ratio Technique (BRT)	7
3 Methodology.....	9
3.1 Description of Hardware.....	10
3.1.1 MoRaP Test Rig & Control System	10
3.1.2 Flat Flame Burner.....	10
3.1.3 Thin Filament Pyrometer	11
3.1.4 Camera & Optics	12
3.1.5 Model Rocket Engine SIE-RCC.....	14
3.2 Measurements	14
3.2.1 Methane-Air Flames	15
3.2.2 Methane-Oxygen Flames	15



3.3	Evaluation	16
3.3.1	Transformation of Flame Images.....	17
3.3.2	Deconvolution of Flame Images	19
3.3.3	Determining Temperature from Radiation Measurement.....	20
3.3.4	Method-1: Calibration Using Reference Temperatures	21
3.3.5	Method-2: Calibration using TFP	23
4	Results & Discussion.....	28
4.1	Method-1: Calibration Using Reference Temperatures.....	28
4.2	Method-2: Calibration Using TFP.....	29
4.3	Comparison of Method-1 & Method-2	32
5	Application to Rocket Engine.....	33
5.1	Differences b/w Current Study & Rocket Engine.....	33
5.1.1	Diffusion Flame	33
5.1.2	Confined Flame	34
5.1.3	High Turbulence.....	34
5.1.4	Higher Pressure	34
5.2	Application of Current Study to Rocket Engine	34
5.3	Further Development	35
5.3.1	Method-A: Modelling Flame Spectra	36
5.3.2	Method-B: Modelling Flame Emissivity.....	37
5.3.3	Considerations for Cavity Radiation	37
5.3.4	Handling Image Noise	37
6	Conclusion.....	38
	References.....	39
	Annexures.....	44
A.1	MATLAB Script for Method-1	44
A.2	MATLAB Script for Method-2	47

List of Figures

Figure 2.1: Example of support for fine-wire thermocouple in an open flame [5].....	3
Figure 2.2: Thin Filament Pyrometer [14]	4
Figure 2.3: Principle of Disappearing Filament Pyrometer [22].....	5
Figure 2.4: Measurement of Flame Emissivity [26].....	6
Figure 2.5: Flame spectrum for a gas-fired furnace [30].....	6
Figure 2.6: Emission spectra for gas molecules in infrared region [21].....	7
Figure 2.7: Illustration of Image Doubler [19].....	8
Figure 3.1: Experimental Arrangement	10
Figure 3.2: Flat flame McKenna burner [45]	11
Figure 3.3: Positioning & mounting arrangement for TFP.....	12
Figure 3.4: Mounting arrangement for camera & optics.....	12
Figure 3.5: Spectral response of camera and optics	13
Figure 3.6: Cross-section of model rocket engine	14
Figure 3.7: Sample pressure measurement for CH4OX-01-FL.....	16
Figure 3.8: Exemplary averaged flame image for point CH4AIR-22-925ND.....	18
Figure 3.9: Plot of intensity profiles at different axial locations for determining angle of rotation.....	18
Figure 3.10: Specimen of deconvoluted flame image	19
Figure 3.10: Specimen for evaluating the goodness of deconvolution.....	20
Figure 3.12: Intensity ratio vs temperature calibration curve generated using methane-air reference flame temperatures.....	22
Figure 3.13: Exemplary fibre images and ratio image for CH4OX-5-FB5 case.....	24
Figure 3.14: Intensity ratio vs flame temperature calibration curve generated using TFP for methane-oxygen flames	27
Figure 4.1: Specimen of temperature distribution determined using method-1 for CH4OX-1-FL.....	28
Figure 4.2: Specimen of axial temperature profiles determined using method-1 for CH4OX-1-FL.....	29
Figure 4.3: Specimen of temperature distribution using method-2 for CH4OX-1-FL	30
Figure 4.4: Specimen of axial temperature profiles determined using method-2 for CH4OX-1-FL.....	30



Figure 4.5: Specimen of temperature distribution using method-2 for CH ₄ AIR-20-FL.....	31
Figure 5.1: Comparison of diffusion & premixed methane flame spectra in the NIR region [56].....	33
Figure 5.2: Specimen of flame image in rocket engine test rig [44]	35
Figure 5.3: Modelled and measured H ₂ O NIR spectra [19].....	36



List of Tables

Table 3.1: Camera settings used for methane-air & methane-oxygen cases.....	15
Table 3.2: Test matrix for methane-air flames.....	15
Table 3.3: Test matrix for methane-oxygen flames	16
Table 3.4: Specimen for selection of cases for evaluation based on error in pressures.....	17
Table 3.5: Intensity ratios for methane-air flames	22
Table 3.6: Polynomial fit coefficients for methane-air calibration curve.....	23
Table 3.7: Comparison of reference & assumed concentrations for CH ₄ O ₂ -1-FL...	25
Table 3.8: Comparison of gas temperature for assumed & reference conc. for CH ₄ O ₂ -1-FL.....	25
Table 3.9: Flame temperatures evaluated using TFP for methane-oxygen flames ..	26
Table 3.10: Polynomial fit coefficients for methane-oxygen calibration curve using TFP.....	27
Table 4.1: Results of method-2 for methane-air flames	32



List of Symbols

Symbol	Description	Unit
d	Diameter	[m]
G	Greyscale signal (intensity)	[count]
h	Convective heat transfer coefficient	[W/m ² .K]
I	Radiation intensity/radiance	[W/m ² .sr]
Nu	Nusselt number	[-]
Re	Reynolds number	[-]
S	Spectral response	[%]
Sc	Scaling factor	[-]
T	Temperature	[K]
ϵ	Epsilon	[-]
λ	Wavelength	[m]
τ	Transmissivity	[-]
ν	Kinematic viscosity	[m ² /s]

Subscripts

f	Fibre
g	Gas/Flame



List of Abbreviations

Abbreviation	Description
CMOS	Complementary Metal Oxide Semiconductor
CFA	Colour Filter Array
Conc.	Concentration
Decon.	Deconvoluted
FBz	Fibre at height z
FL	Flame
FPS	Frames Per Second
FWHM	Full-Width, Half-Maximum
HAB	Height Above Burner
LOS	Line-of-Sight
px	Pixel
Ref.	Reference
RGB	Red, Green, Blue
Temp.	Temperature
TFP	Thin Filament Pyrometer



1 Introduction

1.1 Importance of Flame Temperature Determination

Acquaintance of flame temperature is of prime value in combustion. It is a pointer for flame's heat transfer characteristics, combustion efficiency, and emissions character. Therefore, knowledge of the flame temperature is a first step in designing a combustion system or evaluating the performance of an existing system.

1.2 Project Objective & Scope

The current work aimed at developing a simple system for determination of 2D spatially resolved flame temperature field in a single-injector, oxy-methane model rocket engine. The combustor walls had provision for installing sensor probes (e.g. thermocouples) and a glass window was also provided in it for performing optical measurements.

The scope was limited to test the system by applying it to open-air test flames at atmospheric pressure but at similar fuel-oxidiser conditions as that in the rocket engine. Using this setup, a method was to be devised and possibly a calibration curve was to be developed which could later be applied to the flame in the rocket engine.

2 Literature Review

There are myriad of techniques available for measurement of flame temperature depending upon the type of application. All of them can be broadly characterised as either invasive (probe based) techniques or non-invasive (optical) techniques. There also exist semi-invasive techniques in which medium of interest has to be in contact but remote measurements are possible (e.g. TFP, thermographic phosphors) [1]. Here, only those techniques will be discussed which are relevant to the measurement of flame temperature in our case.

2.1 Probe Methods

The probing methods are those in which the sensor is brought into to physical contact with the flame. Mostly, these techniques are meant for measurement at a point and distributions are obtained by spatial repetition of the measurement. These were relevant for calibrating the flame radiation against known reference temperatures.

2.1.1 Fine Wire Thermocouple

Common types of thermocouples (e.g. K or T type) cannot be used for measuring the high temperatures found in rocket engine flames. However, types S (Pt/Pt10%Rh) and R (Pt/Pt13%Rh) can be used up to 1600 K and type B (Pt6%Rh/Pt13%Rh) up to 1900 K [3]. Special thermocouples based on tungsten and rhenium are available which can measure as high as 2600-3000 K [4]. Based on construction materials, some thermocouples (e.g. R, S, & B) are suitable for inert or oxidising atmospheres while others (e.g. rhenium based) are restricted to reducing atmospheres.

There are various types of probes available for thermocouples but in order to make least impact on the original flow field, exposed junction fine wire (15-150 μm) thermocouples are used. This require special kind of support for holding the thermocouple in the flame, an example is shown in **Figure 2.1** below [5]. Since, sagging of hot thermocouple is a serious problem, spring of calculated stiffness has to be used to keep it under constant tension without breaking.

Various authors have reported using fine-wire thermocouples for flame temperature measurements [6]–[9]. The temperature measured corresponds to thermocouple junction and radiation correction has to be applied for determination of gas temperature. Since geometry of junction plays key role in heat transfer equations, junctions of definite shape can be made through welding. Thermocouples should not be used in regions where soot may be present to avoid changing its surface characteristics. Depending upon the atmosphere, catalysis on the junction surface can cause serious errors which can be avoided by applying an inert coating on the

junction [9], [10]. Moreover, temporal resolution achievable in thermocouple measurements should be considered [11], [12].

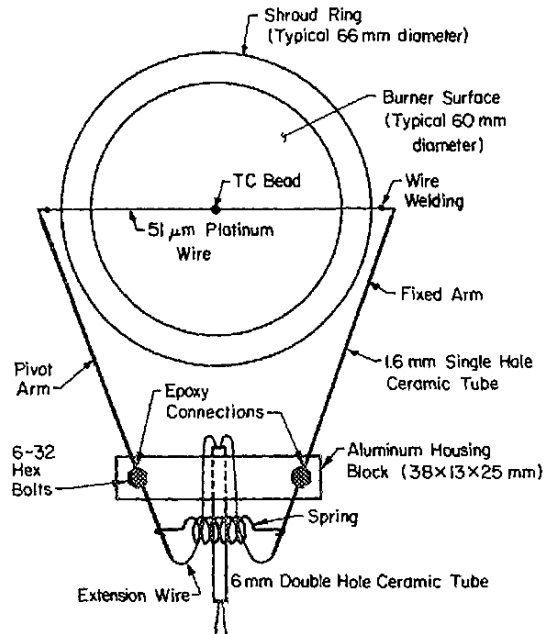


Figure 2.1: Example of support for fine-wire thermocouple in an open flame [5]

2.1.2 Thin Filament Pyrometer (TFP)

The idea is to stretch a fine diameter ceramic wire (fibre) inside the flame as shown in **Figure 2.2** below. By measuring the radiation from glowing fibre, 1D temperature distribution along the fibre can be determined [13]. The camera can either be calibrated e.g. using thermocouple or spectrometer [14]–[16] or calibration can be avoided by measuring the signal in two wavelengths and taking their ratio [6], [17]. The TFP is reported to be more convenient and accurate than the thermocouple measurements [18], [19].

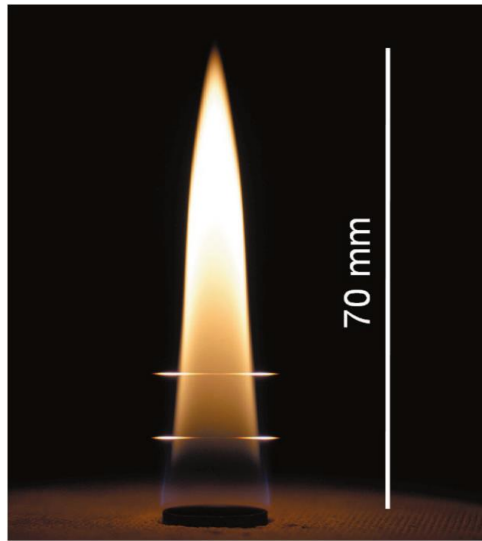


Figure 2.2: Thin Filament Pyrometer [14]

2.2 Optical Methods

There exist numerous optical techniques which can provide accurate measurement of flame temperature [1], [20], [21]. However, most of these techniques e.g. CARS (Coherent Anti-stokes Raman Scattering) and LIF (Laser-Induced Fluorescence) rely on expensive equipment (e.g. lasers, spectrometers) and complicated methods. Therefore, simpler optical techniques based on radiation emission from the flame itself are always sought.

Radiation from flames typically has three parts; thermal radiation from gases in the form of spectral bands, thermal radiation from soot which is continuous and can be approximated by Planck's law, and radiation from intermediate species or radicals due to chemical reactions (chemiluminescence) [2]. Mostly, temperature of a flame is evaluated by measuring the thermal radiation it emits. If the flame is dominated by soot, it is called a sooty (luminous) flame. Else, it is called a non-sooty (non-luminous) flames.

2.2.1 Disappearing Filament Pyrometer

It consist of an electrically heated tungsten filament arranged between the objective lens and the eyepiece (see **Figure 2.3** below) [22]. The target is sighted and filament image is formed superimposed to the target. Current to the filament is adjusted such that its brightness matches with the target and it disappears in the image. Note that it can only measure the brightness temperature and not the true temperature of the target unless its emissivity is known.

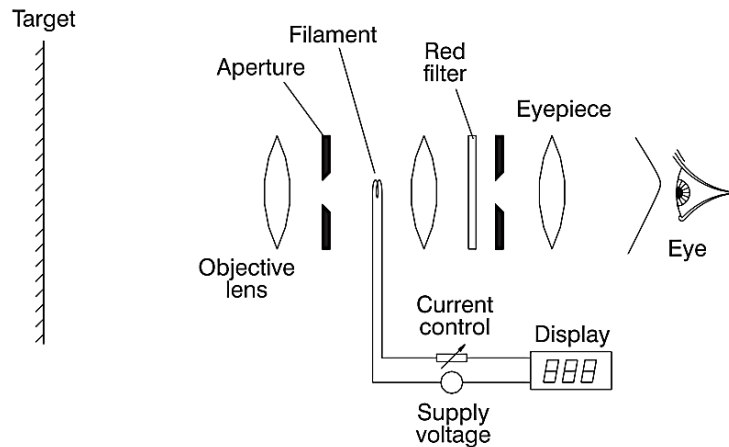


Figure 2.3: Principle of Disappearing Filament Pyrometer [22]

2.2.2 Absolute Camera Calibration

A flame can be imaged using camera to provide the 2D distribution of flame's radiance integrated along line-of-sight and in the spectral range of camera sensitivity. The camera gives relative distribution of radiance and calibration is required to measure the absolute radiation [23], [24]. Using this intensity distribution, the emissivity of the flame can then be theoretically estimated to determine the true temperature [25].

2.2.3 Flame Emissivity Determination using Background Radiation

Main issue in the technique described in § 2.2.2 is predicting the flame emissivity since it is a function of fuel type, temperature, pressure and spatial location. Emissivity of the flame can be indirectly measured by measuring its transmissivity. A radiating background of known temperature and emissivity (e.g. blackbody) is used for this purpose. At least three radiation measurements are made namely; flame-only, background-only, and flame+background combined as shown in **Figure 2.4** below [26]. By using these signals, the transmissivity of the flame can be calculated and using Kirchhoff's radiation law, its emissivity can be determined. The technique can result a point measurement using radiometer [27] or 2D pixel-by-pixel emissivity distribution using IR camera [28] and is applicable to both luminous and non-luminous flames.

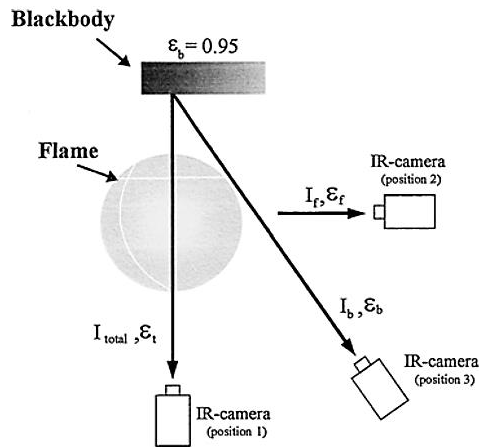


Figure 2.4: Measurement of Flame Emissivity [26]

2.2.4 CO₂ Based Spectral Infrared Thermography

IR camera cannot be directly used to measure the flame temperature. It measures the integrated signal in the spectral range of 3-15 μm [29] in which it will capture a lot of continuous radiation from surrounding in addition to the flame. Furthermore, without any filter, the intense radiation from flame exceeds the upper limit of typically used detector and can cause damage. Flame gases of carbonaceous fuels emit intense radiation in a narrow band centred at 4.25 μm due to CO₂ as shown in **Figure 2.5** below [30]. Using a filter to focus on this band and knowing emissivity of CO₂, flame's true temperature can be determined [31].

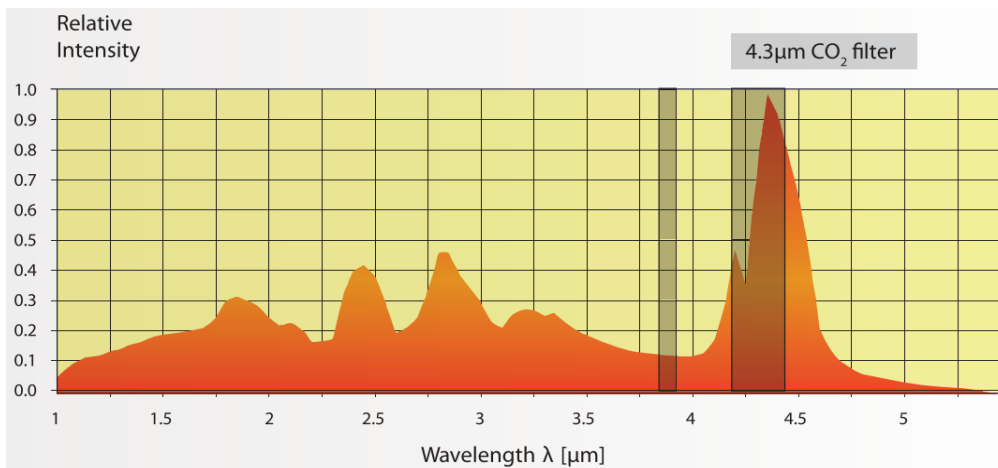


Figure 2.5: Flame spectrum for a gas-fired furnace [30]

2.2.5 Two-Colour Method

Also called quotient or ratio pyrometry, the two colour method (or dual-wavelength thermometry) is focused on measuring radiance (intensity) in two spectral bands and determining their ratio for evaluation of temperature using Planck's law [32]. This technique is applicable only to sooty flames and cannot be directly applied to non-sooty gaseous emissions [33]. At high soot concentrations, very narrow bands close to each other can be used with grey-body assumption so that the emissivity cancels out in the ratio [34]. In other cases, the soot emissivity can be modelled as a function of temperature and wavelength and the two measurements can be used to solve for two unknowns; temperature and emissivity. For this technique, two separate spectral filters can be used [35], [36] or the internal RGB Colour Filter Array (CFA) of the camera can be utilised [37]. In order to improve accuracy, the two spectral bands should lie in a region where slope of Planck's curve is sensitive to temperature. If the calibration constant (multiplier for converting the camera voltages/signal to absolute radiance) is the same for the two spectral ranges, it cancels out in the ratio and there is no need of calibration. However, camera response may not be linear in the selected range in which case it is recommended to perform calibration using a blackbody source of known temperature [33], [34]. The need of calibration can be completely avoided and the accuracy can be increased by using more than two filters. The method is then called multi-wavelength pyrometry [38].

2.2.6 Band Ratio Technique (BRT)

Measurement of the temperature of flames with no or little soot is not possible with the two-colour method since the radiation from a hot gas mixture is non-continuous. Instead, it is in the form of molecular band radiations [21] as shown in **Figure 2.6** below.

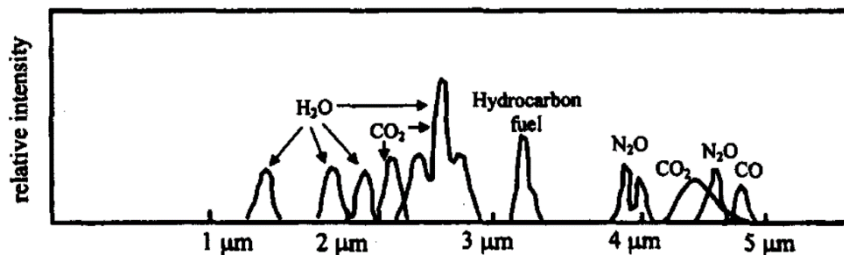


Figure 2.6: Emission spectra for gas molecules in infrared region [21]

It is found that in the near-infrared (NIR) region (0.9-1.7 μm), emission is temperature dependent and is due to the vibration-rotation bands of water only which is the combustion product in all types of flames [39]. This emission can be used to determine the temperature either using a spectroscopic technique or the band ratio technique. Similar to the two-colour method, band ratio technique involves measuring the integrated band intensities in two spectral regions and using its ratio for temperature

evaluation. The emissivity ratio of the gas in the selected spectral bands must either be measured experimentally or modelled theoretically [40]. This technique is also applicable to those flames which have both soot and gas emission, provided both are considered in evaluating the emissivity. The point measurement of the two intensities can be done using spectrometer or radiometer with two spectral filters and 2D measurement can be made using camera with two filters.

Without knowing the emissivity, it is also possible to relate the intensity ratio directly to the temperature either using an emission model [41] or through calibration. Nakaya et al. [19] has recently determined temperatures of premixed flames by imaging in 850-975 nm range and calibrating the intensity ratios to temperatures using a TFP. Note that for transient flames and temporally resolved measurements, images in the two spectral bands should be captured simultaneously. This can be done either by using a beam-splitter and two cameras fitted with two different filters or using a single camera with an image-doubler as shown in the **Figure 2.7** below.

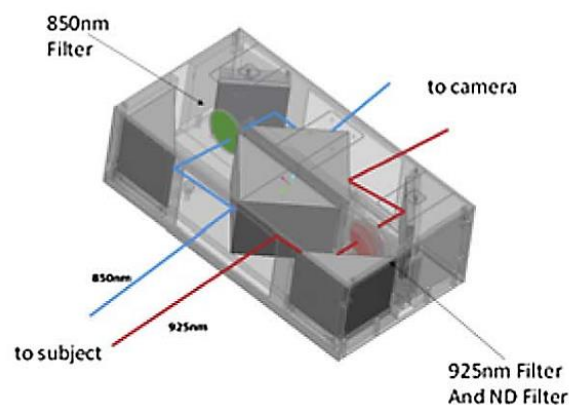


Figure 2.7: Illustration of Image Doubler [19]

3 Methodology

Installation of a sensor probe inside the rocket engine combustor was unfeasible since the probe had to be thin for minimal impact on the flow field. A thin probe (e.g. thermocouple or fibre) would be flimsy and not able to sustain the high gas flowrates typically observed in the combustor. Therefore, optical methods were considered for measuring the flame temperature since a quartz glass window was already available in the combustor.

Controlling the flame background radiation was not possible in the combustor since combustor wall have its own thermal character. Moreover, hardware was unavailable for performing absolute calibration of flame radiation (e.g. Tungsten incandescent calibrated lamp) or any infrared measurements. The flame had little to no soot and therefore two-colour method could not be employed. Thus, band ratio technique was chosen for this study and was tested on open-air flames with methane-air and methane-oxygen as fuel/oxidiser combinations. For calibration of intensity ratio against temperature, two approaches were considered. In method-1, reference temperature values of methane-air flames known from previous DLR experiments were used to develop the calibration curve. Using this curve, temperature fields of methane-oxygen flames were calculated and validated against reference temperatures from previous studies. In method-2, the calibration curve was developed from methane-oxygen flames using TFP measurements. This was then applied to both, methane-oxygen and methane-air flames for validation against temperatures known from literature. The aim was to use these temperature calibrations on the model rocket engine for which no direct calibration could be performed with the available hardware.

Although the target flame flickers due to turbulence, the present study focused at determining a temporally average temperature distribution. Therefore, a single camera was used with sequential replacement of the spectral filters [42], [43]. A review on this topic suggests that sequential imaging has not yet been used for band ratio technique in rocket engine flames. **Figure 3.1** below depicts the schematic for experimental setup used. The open-air burner had a suspended TFP over it and was fed with gases from MoRaP test rig. Flame was imaged through desired spectral filters using a computer-controlled camera. Further details on the hardware are given in the next section.

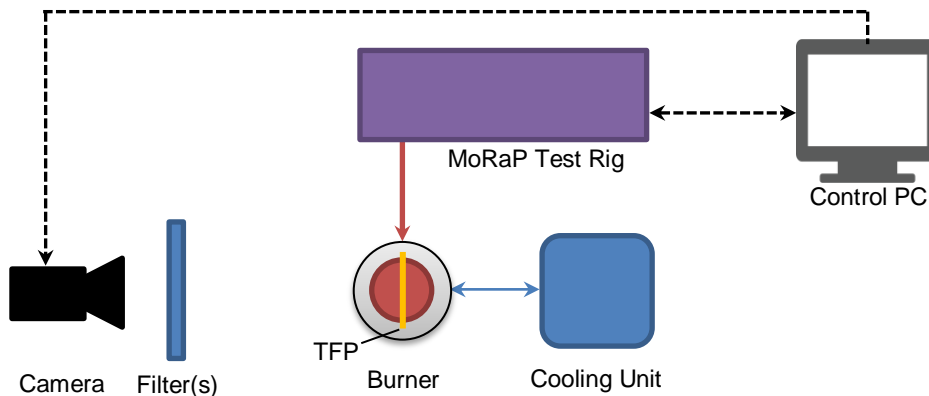


Figure 3.1: Experimental Arrangement

3.1 Description of Hardware

3.1.1 MoRaP Test Rig & Control System

MoRaP is a generic Model Rocket Engine Test Rig available in the laboratory for testing of engines/burners and is equipped with control valves, pressure regulators, pressure transducers, feed lines and connectors. It was used to supply gases from pressurised gas cylinders to the open-air burner in a controlled manner. The flowrate of gases was controlled indirectly through pressure regulators and sonic orifices. Pressure transducers were used to measure the actual pressures of streams fed into the burner.

The test rig has multiple National Instruments Inc. data acquisition cards (DAQ devices) which are wired to the control computer via Local Area Network (LAN). An already developed LabVIEW Virtual Instrumentation (VI) panel was used to control the experiments and record the data.

3.1.2 Flat Flame Burner

The McKenna flat flame burner [45] (see **Figure 3.2** below) has been used in the labs as a standard calibration burner due to its reproducibility [46]. Several previous studies have already been done using this burner which can serve as a reference and therefore it was selected. The burner had a sintered bronze disc in diameter of 60 mm and shroud ring inner/outer dimensions of 62/74 mm. The gases were mixed in a mixing tee ~1.5 m upstream of the burner to make sure that the flame is premixed. The cooling unit was set to provide a fixed cooling water supply temperature of 16° C.

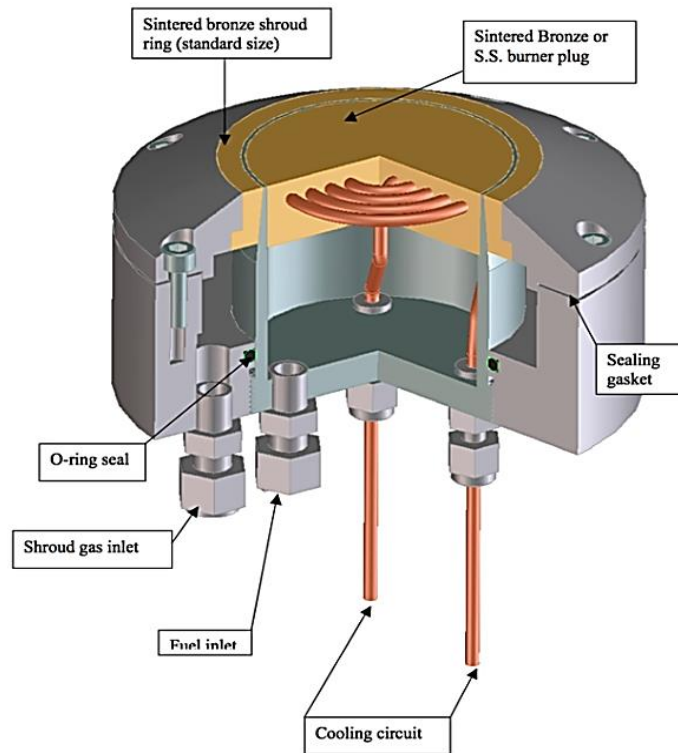


Figure 3.2: Flat flame McKenna burner [45]

3.1.3 Thin Filament Pyrometer

In the previous studies mentioned in § 2.1.2, a single filament $\sim 14 \mu\text{m}$ diameter SiC fibre (tradename CG Nicalon) was used. As an alternate, a much cheaper fibre called CeraFib 75 (75% Al_2O_3 , 25% SiO_2) manufactured by CeraFib GmbH, Germany [47] was utilised in this study. This fibre has not yet been reported for use as a TFP in the literature. The fibre had multiple filaments with a diameter of $12 \mu\text{m}$ and melting point of 2100 K. Since it was not possible to separate out a single filament from the thread/fibre, its diameter was reduced as much as possible by using a blade knife. Average diameter of the resulting fibre was $\sim 36 \mu\text{m}$. **Figure 3.3** below shows the scaling and mounting of the fibre. The fibre was positioned at the centre of the burner disc manually at the desired Height-Above-Burner (HAB). Optically non-reflecting tape was used to avoid reflections from nearby supports.

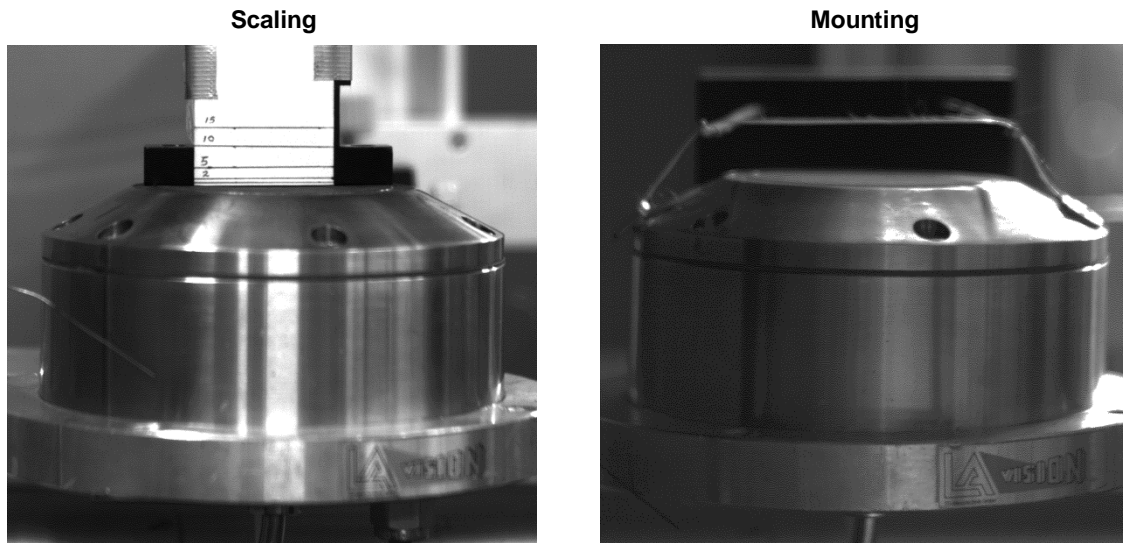


Figure 3.3: Positioning & mounting arrangement for TFP

3.1.4 Camera & Optics

A greyscale CMOS camera (model BU205M) manufactured by Toshiba Teli Corporation, Japan was employed. The camera had a resolution of 2048 x 1088 (sensor array size 11.26 mm x 5.98 mm) and a maximum shutter speed of 170 FPS. It was fitted with a C-mount prime objective lens of 25 mm focal length with a maximum aperture of F/1.4. The camera was connected to the PC via USB interface and vendor's software was used to acquire 8-bit images (greyscale values 0-255) in the desired exposure.



Figure 3.4: Mounting arrangement for camera & optics

All the optics were mounted on an optical bench as shown in **Figure 3.4** above. 25 mm diameter filters manufactured by Edmund Optics Inc. were used with wavelengths centred at 850 nm and 925 nm and FWHM of 25 nm since these wavelengths were

already tested for NIR thermometry as mentioned in [19]. The filters were sequentially mounted in a filter holder placed in front of the camera. The H₂O emission in 925 nm range is much higher than in 850 nm. This causes a problem since either the image saturates in 925 nm range or very weak signal is captured in 850 nm range. To make them comparable, a neutral density filter with optical density of 0.6 (transmissivity ~25%) was used along with 925 nm filter for imaging the flame. However, this ND filter was not required for TFP since its emission did not differ very much in the two spectral bands.

Figure 3.5 below depicts the spectral response of the optics and the combined spectral response in the two measurement bands. Since the bands are narrow, mean values for spectral responses were considered to determine the spectral response ratios as follows:

$$S_{850}/S_{925} = 1.8563, \quad S_{850}/S_{925ND} = 7.8899 \quad (3.1)$$

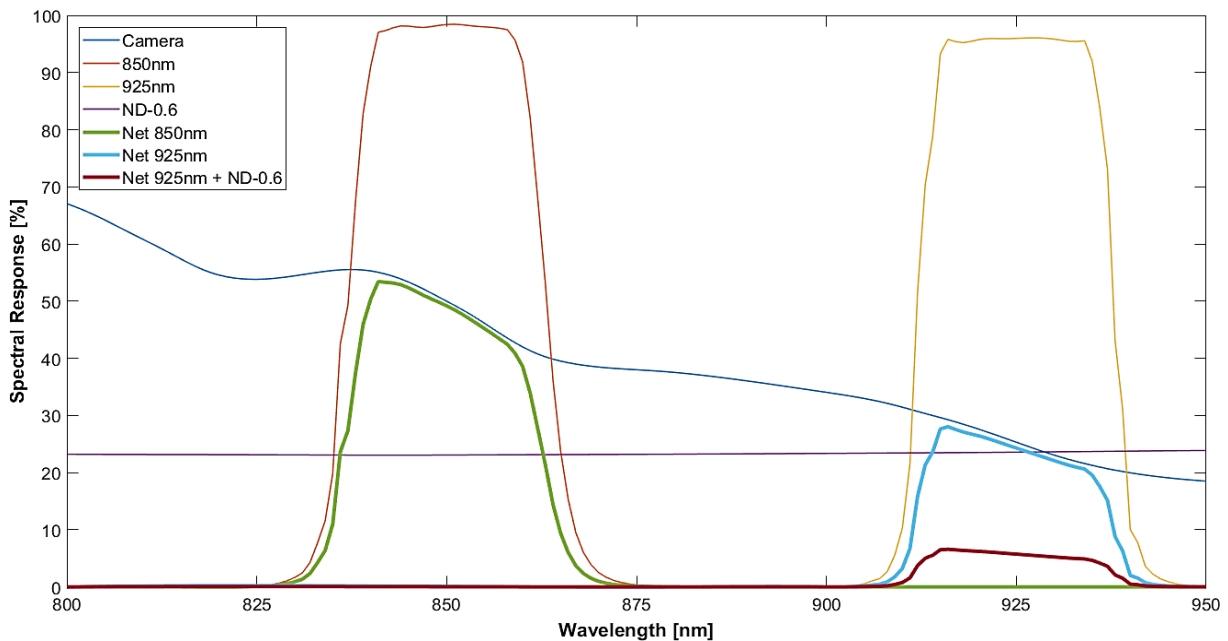


Figure 3.5: Spectral response of camera and optics

3.1.5 Model Rocket Engine SIE-RCC

The rocket engine for which this measurement method was developed is a Single Injector Element Rectangular Combustion Chamber (SIE-RCC). It consists of a 12 mm x 12 mm, 290 mm long combustor made from oxygen-free copper (cross-section shown in **Figure 3.6** below.) It is fitted with a shear coaxial injector in which gaseous oxygen is supplied through a central nozzle (diameter 4 mm) while gaseous methane is provided in the surrounding annulus (outer diameter 6 mm). Multiple thermocouples are installed in the combustor walls. A 12 mm x 40 mm quartz glass window is provided at the top. Gases at ambient temperature are supplied from pressurised cylinders via MoRaP test rig. Measurements are usually done in the pressure range of 10-20 bar with fuel equivalence ratio in the range 1.18-1.8. Further details can be found in [44].

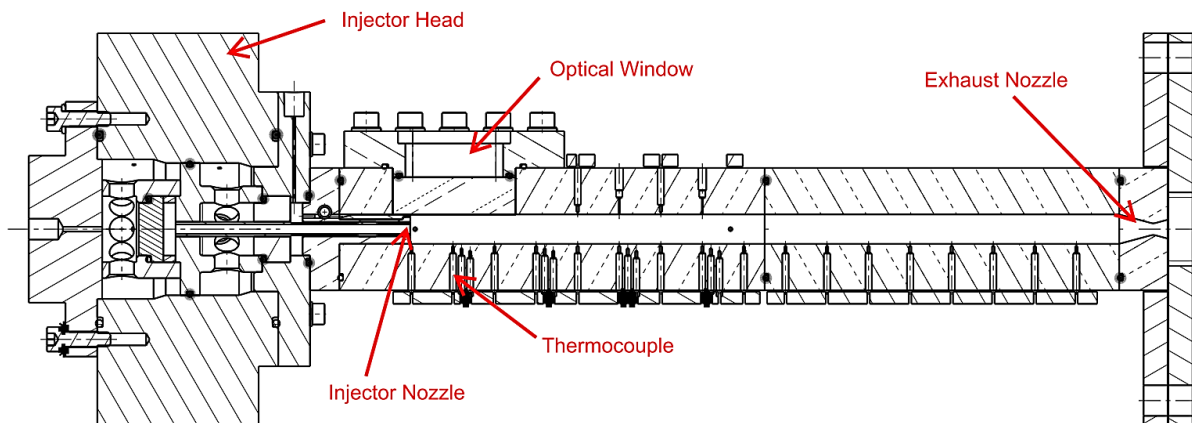


Figure 3.6: Cross-section of model rocket engine

3.2 Measurements

In order to set the desired flowrates, the pressures were calculated using an already available spreadsheet based on gas-dynamics equations. The pressures were physically set for each operating point using pressure regulators. The sequence was then run from LabVIEW panel for the desired duration and the flame was ignited using a butane lighter at the start of each sequence. The measurement values for all sensors were recorded in a sequence file as a function of time.

Duration for all the sequences was kept as 30 s. After setting the operating pressures, the flame was imaged in two spectral bands, 850 nm and 925 nm + ND-0.6, for both methane-air and methane-oxygen flames. The TFP was used only for methane-oxygen case and was imaged in spectral bands 850 nm and 925 nm. **Table 3.1** below summarises the camera conditions used. Note that FPS varies with the exposure setting but is not important since only temporally averaged images were of interest.

Table 3.1: Camera settings used for methane-air & methane-oxygen cases

	Methane-Air		Methane-Ox		
	Flame (850 & 925ND)	Fibre (850 & 925)	Flame (850 & 925ND)	Fibre (850 & 925)	
HAB [mm]	-	15	-	2, 5	10, 15
Exposure [μs]	60,000	800	35,000	2,000	10,000
Aperture [F No.]	F/2	F/2	F/2	F/2	F/2
Gain [x]	0	0	0	0	0
Duration [s]	30	30	30	30	30
Frames used for Averaging	350	1000	550	1100	1100

Maximum FPS: 170

3.2.1 Methane-Air Flames

Although the target rocket engine flame is methane-oxygen, tests were also performed for methane-air flame since adequate reference data was available for it in contrast to methane-oxygen. For McKenna burner, temperature of methane-air flame at Height-Above-Burner (HAB) of 15 mm were measured by Weigand et al. at DLR (German Aerospace Centre) for a variety of operating conditions using CARS [48]. Operating points listed in **Table 3.2** were selected for study. Since there was no air supply available for the desired pressures, air was assumed to be 79% N₂, 21% O₂ mixture by mole and the two gases were supplied to the mixing tee from different gas cylinders.

Table 3.2: Test matrix for methane-air flames

DLR Case No.	CH4		Air				Total			Remarks
	Flow		Flow		O2	N2	Flow	Eq. Ratio	A/F Ratio	
	[slpm]	[g/s]	[slpm]	[g/s]	[g/s]	[g/s]	[g/s]	-	-	
6	1.420	0.0169	15.000	0.3232	0.0753	0.2479	0.3401	0.900	19.073	
8	1.733	0.0207	16.500	0.3555	0.0828	0.2727	0.3762	1.000	17.191	
20	2.550	0.0304	17.430	0.3755	0.0875	0.2880	0.4059	1.390	12.341	
22	3.420	0.0408	32.400	0.6980	0.1627	0.5354	0.7389	1.000	17.105	

Ambient Pressure = 1 bar, Ambient Temperature = 288 K, HAB = 15 mm

3.2.2 Methane-Oxygen Flames

Xu et al. has reported temperature and species concentration measurements of methane-oxygen flame using McKenna burner [49]. All the tested flames were rich (like in the target flame of model rocket engine) and contained some soot at HAB>5 mm. Gas temperatures in the soot-free zone close to the burner surface were measured using S-type thermocouple while the soot temperatures (assumed to be equal to the gas temperatures) at higher locations were measured with two-line (similar to two colour) method.

In addition to reference conditions (case 1), we also did measurements for stoichiometric and lean conditions. In all the cases, shielding nitrogen gas flow was maintained at 0.1643 g/s. For each operating point, TFP was imaged at HAB of 2, 5, 10, 15 mm.

Table 3.3: Test matrix for methane-oxygen flames

S/N	CH ₄		O ₂		N ₂ Shielding	Total Excluding Shielding Gas			Remarks
	Flow	Flow	Flow	Flow	Flow	Flow	O/F Mass Ratio	Fuel Eq. Ratio	
	[g/s]	[m ³ /s]	[g/s]	[m ³ /s]	[g/s]	[g/s]	[-]	[-]	
1	0.0401	5.60E-05	0.1392	9.75E-05	0.164	0.1793	3.471	1.15	Reference
3	0.0423	5.91E-05	0.1349	9.45E-05	0.164	0.1772	3.189	1.25	Reference
4	0.0408	5.70E-05	0.1627	1.14E-04	0.164	0.2035	3.988	1.00	
5	0.0408	5.70E-05	0.1061	7.43E-05	0.164	0.1469	2.600	1.54	
6	0.0304	4.25E-05	0.1355	9.49E-05	0.164	0.1659	4.457	0.90	Flame Only

Ambient Pressure = 1 bar, Ambient Temperature = 292 K, HAB = 2, 5, 10, 15 mm

3.3 Evaluation

The pressure regulators available in the MoRaP test rig were suitable for high pressures in the range of 0-100 bar. For pressure range of 5-10 bar, the precision of these regulators was inappropriate. This caused errors in the gas flowrates for some operating points. A script was formulated using MATLAB vR2017a for reading the sequence file and evaluating the mean pressures measured by the transducer, example of methane pressure for CH₄OX-01-FL (methane-oxygen, operating point 1, flame) is shown in **Figure 3.7** below.

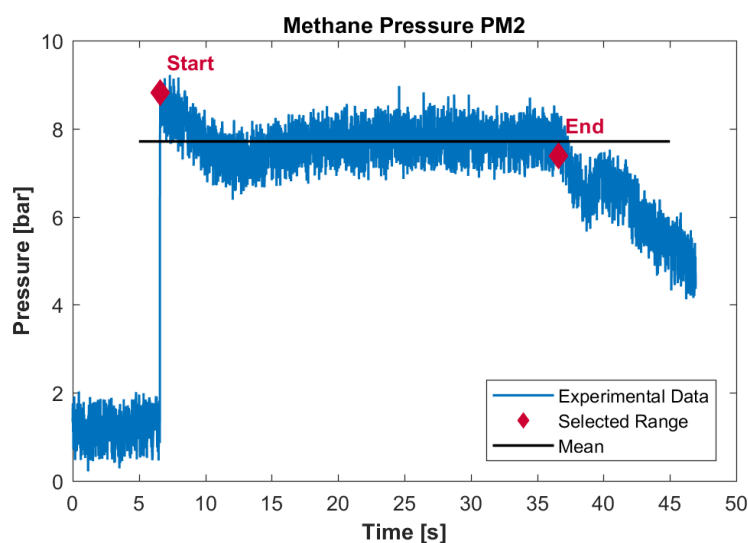


Figure 3.7: Sample pressure measurement for CH₄OX-01-FL

The percentage error between the desired/calculated (p_{calc}) and actual (p_{act}) supply pressures was calculated as:

$$\Delta p_{err}(\%) = 100 \cdot \frac{|p_{act} - p_{calc}|}{p_{calc}} \quad (3.2)$$

This error was found to be different for different cases. An error in pressure directly produces an error in the flowrate which would be propagated further to cause an error in resulting temperatures. Therefore, measurements with pressure error more than 10% were discarded and hence the operating conditions (pressure/flowrate) for remaining data was in error of no more than 10%. Error in shielding N_2 was not considered. **Table 3.4** below shows an exemplary case of CH4OX-1 in which four measurements were selected and one was rejected based on this error evaluation.

Table 3.4: Specimen for selection of cases for evaluation based on error in pressures

Test	Pressure [bar]									Output Pair
	Shielding N_2			Oxygen			Methane			
	Calc.	Actual	Error [%]	Calc.	Actual	Error [%]	Calc.	Actual	Error [%]	
2018-11-22-TCR-01-15-30-01-3-FL-925ND	3.63	3.41	6.15	8.76	9.03	3.09	7.88	7.83	0.64	CH4OX_01-FL
2018-11-22-TCR-01-15-30-01-4-FL-850	3.63	3.41	6.03	8.76	9.03	3.05	7.88	7.66	2.75	
2018-11-22-TCR-01-15-30-01-5-FB2-925	3.63	3.89	7.22	8.76	8.95	2.21	7.88	7.74	1.77	CH4OX_01-FB2
2018-11-22-TCR-01-15-30-01-6-FB2-850	3.63	3.92	7.98	8.76	8.99	2.66	7.88	7.31	7.23	
2018-11-22-TCR-01-15-30-01-7-FB5-850	3.63	3.92	8.12	8.76	8.98	2.46	7.88	7.14	9.40	CH4OX_01-FB5
2018-11-22-TCR-01-15-30-01-8-FB5-925	3.63	3.98	9.59	8.76	9.01	2.88	7.88	7.61	3.47	
2018-11-22-TCR-01-15-30-01-9-FB10-925	3.63	6.47	78.28	8.76	10.94	24.90	7.88	7.92	0.46	CH4OX_01-FB10
2018-11-22-TCR-01-15-30-01-10-FB10-850	3.63	4.10	12.90	8.76	9.01	2.83	7.88	7.66	2.82	
2018-11-22-TCR-01-15-30-01-11-FB15-850	3.63	4.38	20.60	8.76	8.85	0.98	7.88	7.61	3.38	CH4OX_01-FB15
2018-11-22-TCR-01-15-30-01-12-FB15-925	3.63	4.38	20.60	8.76	8.85	0.98	7.88	7.61	3.38	

Output pairs highlighted in yellow were selected for study

3.3.1 Transformation of Flame Images

For each operating point, the starting and ending frames for stable combustion were manually identified and then a MATLAB script was used to determine the average image from the frames in between them. A sample of average flame image is given in **Figure 3.8** below. The scales for the images were determined using the scaling images as shown in **Figure 3.3** and then comparing the distance in millimetres to that in number of pixels using Inkscape v0.92 software. The scales (px/mm) were found to be:

$$S_{CH_4Air} = 121/15, S_{CH_4OX} = 101/13 \quad (3.3)$$

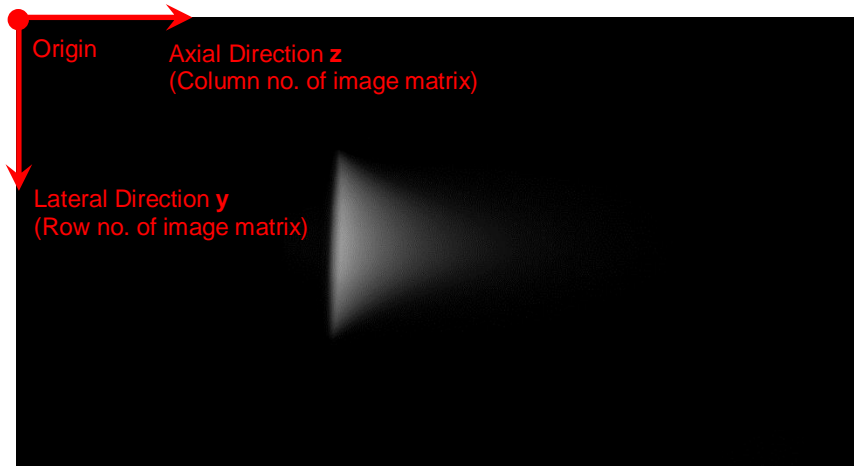


Figure 3.8: Exemplary averaged flame image for point CH4AIR-22-925ND

Since the imaged flame was not truly vertical due to misalignment in camera mounting, all the images had to be rotated. In order to determine the angle of deviation from true vertical, the intensity profiles along lateral direction were plotted and fitted with a 4th degree polynomial at 3 axial locations as shown in **Figure 3.9** below. This resulted in an angle of 1° and all the averaged images were rotated anti-clockwise by this angle using MATLAB.

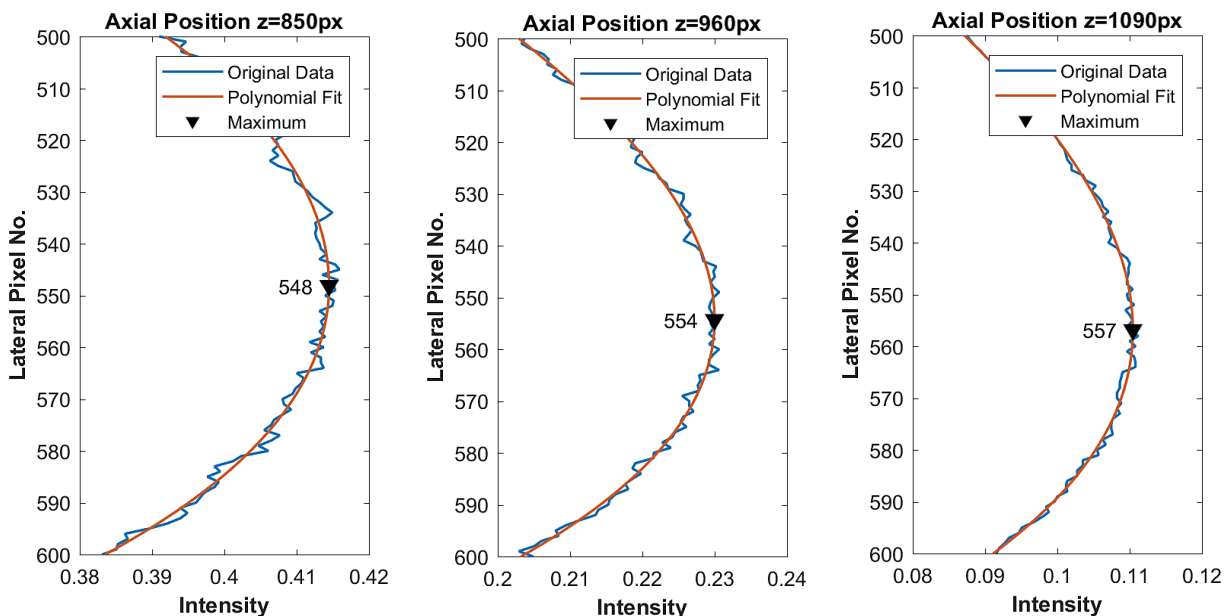


Figure 3.9: Plot of intensity profiles at different axial locations for determining angle of rotation

After rotation, same script as above was used to determine the central pixel location which was found to be $y=532$ px for methane-air and $y=530$ px for methane-oxygen case. Using the scaling factor and this central axis, all the averaged images were cropped using MATLAB for a size of 60 mm x 100 mm such that the burner base coincides with $z=0$ mm location.

3.3.2 Deconvolution of Flame Images

All the reference temperatures known from previous studies were determined at central axis of the burner. The images captured by the camera in this study were Line-of-Sight (LOS) integrated images and therefore deconvolution was mandated. However, if intensity ratio along central plane would be the same as for LOS images, this would be advantageous for eliminating the need of deconvolution. Since this could only be established after comparing the two intensity ratios, deconvolution was considered for exemplary cases. All images were deconvoluted through Inverse Abel Transform using Fourier algorithm implemented in a MATLAB script as described in [50]. Each image was folded along its centreline and the two halves were averaged before deconvolution for symmetrising. This is reported to produce better results [17]. **Figure 3.10** below shows a specimen for a deconvoluted flame image for case CH4AIR-22-FL, intensity is scaled in 0-1 range for both the images.

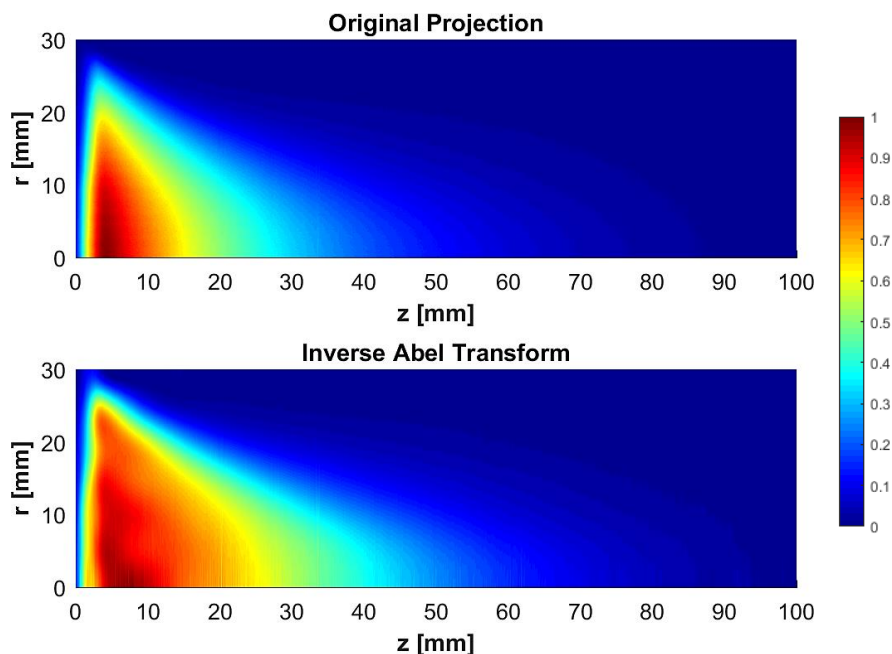


Figure 3.10: Specimen of deconvoluted flame image

The deconvoluted image was unfolded again to develop the full flame image. The goodness of this method was evaluated by fitting the lateral intensity profiles of the deconvoluted image using a polynomial and then applying Forward Abel Transform to

it. The reproduced projection was compared with the original projection, an example for 1D comparison at $z=HAB=15$ mm is shown in **Figure 3.11** below. Best results were obtained with lower frequency of 1 and upper frequency of 6 for the Fourier series.

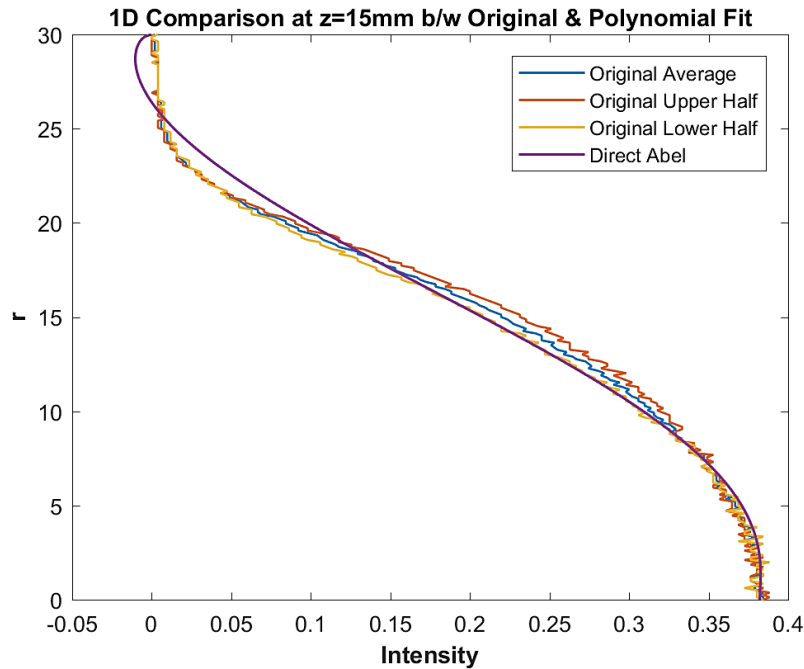


Figure 3.11: Specimen for evaluating the goodness of deconvolution

Note that deconvolution was not necessary for fibre images as they were already located in the central plane.

3.3.3 Determining Temperature from Radiation Measurement

The voltages measured at each pixel of the camera sensor array are converted and recorded as an 8-bit digital greyscale signal (an integer in 0-255 range). This signal “ G ” is related to the actual radiance “ I ” by [37], [51]:

$$G(\lambda, T) = R \cdot S(\lambda) \cdot \tau(\lambda, T_{amb}) \cdot I(\lambda, T) \quad (3.4)$$

Where;

R = Calibration constant for converting radiance to greyscale

S = Combined spectral response of camera & optics

τ = Atmospheric transmissivity

λ = Wavelength

T, T_{amb} = Flame temperature, ambient temperature

It means that the original radiance is altered by spectral characteristics of the camera, optics, and atmosphere. Note that when taking the ratio of two signals (as in two colour or band ratio technique), the calibration constant and atmospheric transmissivity cancels out as they remain the same in the two spectral bands. Similarly, the effect of shielding nitrogen in methane-oxygen flames also cancels out. The radiation intensity is related to temperature and wavelength by Planck's law. Since Planck's equation is difficult to solve explicitly for temperature, it is approximated very well by Wien's distribution law at smaller wavelengths (encountered in our case) which is given by [33],:

$$I = \epsilon(\lambda, T) \cdot \frac{C_1}{\lambda^5} \cdot e^{-C_2/\lambda T} \quad (3.5)$$

Where;

$$\begin{aligned} \epsilon &= \text{Emissivity} \\ C_1 &= 3.7418 \times 10^{-16} \text{ W} \cdot \text{m}^2 && \text{(First Planck's constant)} \\ C_2 &= 1.4388 \times 10^{-2} \text{ m} \cdot \text{K} && \text{(Second Planck's constant)} \end{aligned}$$

For soot, the emissivity depends upon wavelength and temperature but for gases, it also depends upon the product of partial pressures (or concentration) and optical path length (pL). Inserting the Wien's formula into equation (3.4) for the two signals, taking the ratio, and solving for temperature gives:

$$T = \frac{C_2 \cdot \left(\frac{1}{\lambda_2} - \frac{1}{\lambda_1} \right)}{\ln \left(\frac{G_1}{G_2} \right) + \ln \left(\frac{S_2}{S_1} \right) + \ln \left(\frac{\epsilon_2}{\epsilon_1} \right) + \ln \left(\frac{\lambda_1}{\lambda_2} \right)^5} \quad (3.6)$$

The ratio of spectral response (S_2/S_1) is called instrument factor and can be determined from spectral responses of the camera & optics or it can be determined experimentally through calibration [34]. This has already been calculated from the vendor's data as given in equation (3.1). Equation (3.6) is applicable to both the non-sooty gas flames (band ratio technique) and sooty flames or TFP (two-colour method). Since emissivity ratio for the former is unknown and varies with operating conditions, we will only use this formula for TFP for which grey-body assumption is valid and this ratio is 1.

3.3.4 Method-1: Calibration Using Reference Temperatures

In this method, intensity ratios for methane-air flames were calculated and calibrated against the DLR reference temperatures. This calibration was then applied to methane-oxygen flames. A MATLAB script given in annexure A.1 on p. 44 was used for evaluating the methane-air intensity ratio images (G_{850}/G_{925ND}) from the averaged images, all of them were <1 . The infinity and non-number (NaN) values were set to

zero. The intensity ratio was determined at HAB=15 mm along the centreline by averaging values in a box of 3 x 3 pixels (~ 0.37 mm x 0.37 mm). **Table 3.5** below summarises the resulting values along with the reference temperatures at that location for the LOS and deconvoluted (Decon.) images.

Table 3.5: Intensity ratios for methane-air flames

Case	HAB [mm]	Intensity Ratio (850/925ND)		Reference Temp. [K]
		LOS Flame	Decon. Flame	
6	15	0.275794	0.278964	1799
8	15	0.433715	0.479158	1886
20	15	0.507893	0.519765	1929
22	15	0.602478	0.605962	2100

Using these values, a calibration curve was developed by fitting a 2nd degree polynomial equation as shown in **Figure 3.12** below. The coefficients of polynomial equation are given in **Table 3.6**. It is clear that at a given temperature, deconvoluted flame images have slightly higher ratio than LOS flame images.

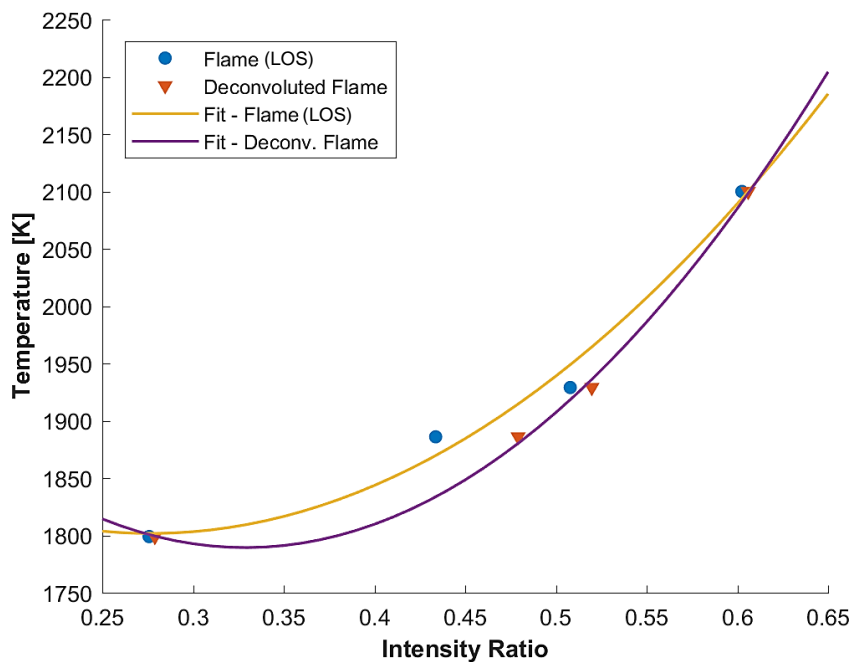


Figure 3.12: Intensity ratio vs temperature calibration curve generated using methane-air reference flame temperatures

Table 3.6: Polynomial fit coefficients for methane-air calibration curve

	Polynomial Coefficients		
	a1	a2	a3
LOS Flame	2749.191	-1520.43	2011.918
Decon. Flame	4023.831	-2646.51	2224.517

Water is produced not only in methane-air but also in methane-oxygen flames with essentially the same NIR spectral distribution. The only difference between the two is the presence of nitrogen in methane-air flames which causes cooling and lower absolute radiant intensities [52]. Nitrogen oxides and radicals produced if any would not emit in the NIR region and intensity ratio would not be affected. Furthermore, small content of soot if present in the region of investigation would not be significantly different in the two flames. Therefore, we could expect the same calibration curve to be applicable to both the flames. A similar argument was validated by Nakaya et al. [19] for CO₂. He showed that calibration curve developed for H₂-air flames was also valid for methane-air flames since CO₂ had no impact in this NIR range.

3.3.5 Method-2: Calibration using TFP

In this approach, we measured the methane-oxygen flame temperatures using TFP at 4 different heights for each operating condition and used this data to calibrate the intensity ratio of flames to the temperature. This calibration was then applied to both, methane-oxygen and methane-air flames. For a given operating point and location, the fibre was imaged with 850 nm and 925 nm filters. Another MATLAB script given in annexure A.2 on p. 47 was developed for this method. Since the fibre images also contained LOS flame radiation, the flame-only images were subtracted from the fibre+flame images. However, the exposures of the flame images and fibre+flame images were different since ND filter with 925 nm was used for former but not for latter. They were balanced by evaluating the flame brightness at a fixed location in the two images and determining a multiplication factor for the flame-only images. After multiplying the flame-only images with this factor, they were subtracted from fibre+flame images to obtain the fibre-only images. The intensity ratio (G_{850}/G_{925}) image was constructed for the fibre which contained values greater and less than 1. NaN and infinity values were again set to zero, specimen is shown in **Figure 3.13**. Note that the glow of fibre is much wider than its original thickness as also observed by other researchers [15]. This is partly due to difference in lens focus setting for 850 & 925 nm fibre images and partly due to glow of tiny filament fragments around the fibre since it was not perfectly smooth. Blooming/streaking due to optics may also be a contributor to it but could not be verified. The value of ratio was determined by taking mean for a 3 x 3 pixels box located at the intersection of the centreline of the fibre and the burner axis.

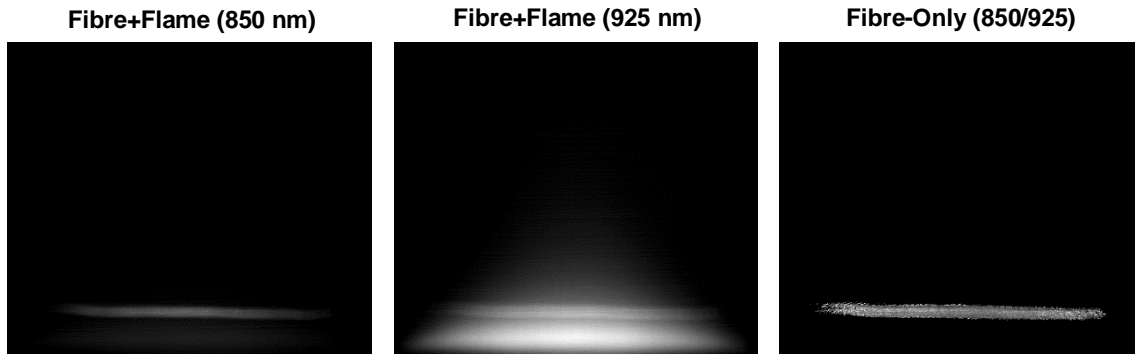


Figure 3.13: Exemplary fibre images and ratio image for CH4OX-5-FB5 case

Using this ratio and grey-body assumption in equation (3.6), temperature of the fibre was determined. In order to calculate the gas/flame temperature, an energy balance for the fibre was considered in which it gains heat from the flame through convection and loses it to the surrounding through radiation [6], [19]. The gas temperature is then given by:

$$T_g = \frac{\epsilon_f \cdot \sigma \cdot (T_f^4 - T_{amb}^4)}{h} + T_f = \frac{\epsilon_f \cdot \sigma \cdot (T_f^4 - T_{amb}^4)}{(Nu \cdot k_g / d_f)} + T_f \quad (3.7)$$

Where,

ϵ_f = Emissivity of the fibre	σ = Stefan-Boltzmann constant
d_f = Fibre diameter	h = Convection coefficient
T_f = Fibre temperature	Nu = Nusselt number
T_{amb} = Ambient temperature	k_g = Thermal conductivity of gas

The fibre acts as a cylinder in an external flow. Following correlation for Nusselt number was used from [53]:

$$Nu = C \cdot Re^m \quad (3.8)$$

Where,

$Re = d_f \cdot U_0 / \nu$ (Reynolds number)
ν = Kinematic viscosity of gas
$C = 0.565$ ($0.004 < Re < 0.09$), 0.80 ($0.09 < Re < 0.01$)
$m = 0.136$ ($0.004 < Re < 0.09$), 0.28 ($0.09 < Re < 0.01$)

The Re was found to be of the order of 0.004 and therefore $C = 0.565$, $m = 0.136$ were chosen. Emissivity of the fibre was not available from the manufacturer. Since it was made from 75% alumina and 25% silica, their emissivities were used from literature.

Both were in the range of 0.04-0.06 for temperatures in the range of 1500-2000 K [54]. A value of 0.06 was used for all the cases. Soot, if any, would be too low at the probed locations and was assumed to have no impact on the fibre.

Thermal conductivity and the kinematic viscosity were calculated at the fibre temperature by considering gas as a mixture of different components using Aspen Plus v9 software. The concentrations of different components were known from reference but only for specific locations. In order to simplify the calculations, these two properties were evaluated by assuming half-way reaction for all cases. The concentrations for half-way reaction and reference condition are given in **Table 3.7** below.

Table 3.7: Comparison of reference & assumed concentrations for CH4OX-1-FL

	Molar Concentrations [%]							
	CH ₄	O ₂	H ₂ O	CO ₂	H ₂	C ₂ H ₂	C ₂ H ₄	CO
Complete Combustion	1.000	2.000	2.000	1.000	0.000	0.000	0.000	0.000
Products at End of Reaction	0.000	0.000	0.667	0.333	0.000	0.000	0.000	0.000
Half-Way Reaction	0.167	0.333	0.333	0.167	0.000	0.000	0.000	0.000
Ref. Concentration @ 15 mm	0.050	0.000	0.420	0.109	0.420	0.015	0.004	0.355

The gas temperature calculated by assuming half-way reaction was compared to that computed from reference concentrations. Results for CH4OX-1-FL case are summarised in the **Table 3.8** below. Since there was no significant difference, assumed concentrations were used for rest of the cases.

Table 3.8: Comparison of gas temperature for assumed & reference conc. for CH4OX-1-FL

	T _f	Total Flow	U ₀	v _g	k _g	Re	C	m	Nu	h	T _g	T _{ref}	Error
	[K]	[m ³ /s]	[m/s]	[m ² /s]	[W/m.K]	[-]	[-]	[-]	[-]	[W/m ² .K]	[K]	[K]	[%]
Assumed Conc.	1959.99	1.53E-04	0.05	4.37E-04	1.83E-01	0.004477	0.565	0.136	0.27	1376.29	1996.45	1771.40	12.70
Reference Conc.	1959.99	1.53E-04	0.05	6.67E-04	3.19E-01	0.002929	0.565	0.136	0.26	2262.79	1982.16	1771.40	11.90

The procedure of determining gas temperature from intensity ratio of TFP was first validated against the reference temperatures for CH4OX-1 case, example shown in **Table 3.8** above. The validation error in calculated temperature (T_{calc}) with respect to reference temperature (T_{ref}) was calculated as:

$$\Delta T_{err}(\%) = 100 \cdot \frac{|T_{ref} - T_{calc}|}{T_{ref}} \quad (3.9)$$

The maximum validation error was found to be 12%. This is a cumulated error, resulting partly due to error in pressure setting and partly due to error in filament pyrometry. Since the fibre consist of multiple filaments, the intensity ratio had some inhomogeneity contributing to this error. After validation, the TFP temperatures were evaluated for all other cases. For some cases, the fibre inhomogeneity was very high resulting in erroneous temperatures (too high or negative.) After discarding those erroneous temperatures, following data was generated:

Table 3.9: Flame temperatures evaluated using TFP for methane-oxygen flames

Case	HAB [mm]	Intensity Ratio			Fibre	Flame
		Fiber 850/925	LOS Flame 850/925ND	Deconv. Flame 850/925ND	T _f [K]	T _g [K]
1	15.45	1.41	0.37	0.41	1959.99	1996.45
5	15.70	1.42	0.44	0.49	1990.61	2029.54
1	5.53	1.47	0.57	0.60	2087.68	2132.60
3	12.10	1.52	0.67	0.75	2216.16	2270.90

Using this data, a calibration curve was developed between temperature and intensity ratio of flame images by fitting it with a polynomial of 2nd degree. **Figure 3.14** below shows the calibration curve and the coefficients of polynomial are given in **Table 3.10**. Note that this calibration curve should also be valid for the methane-air flames due to the reasons given in §3.3.4.

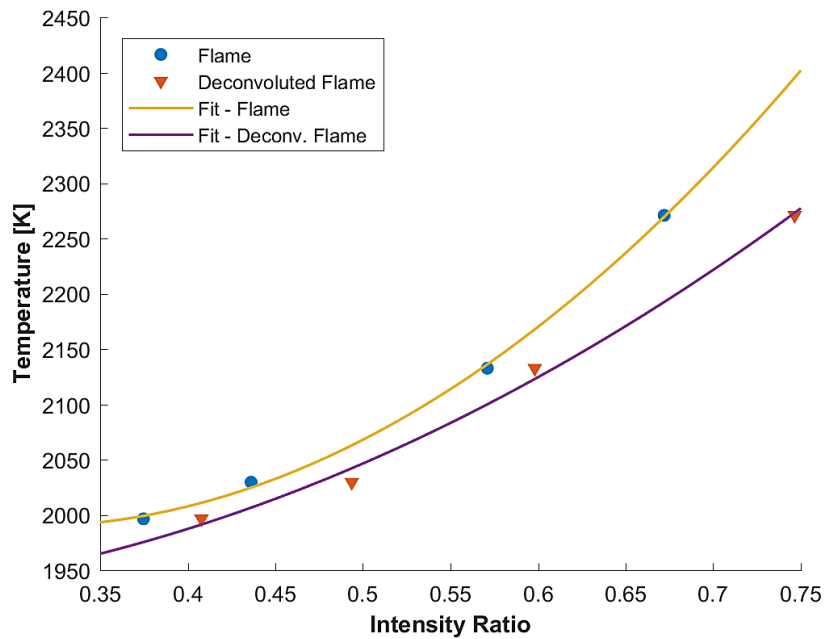


Figure 3.14: Intensity ratio vs flame temperature calibration curve generated using TFP for methane-oxygen flames

Table 3.10: Polynomial fit coefficients for methane-oxygen calibration curve using TFP

	Polynomial Coefficients		
	a1	a2	a3
LOS Flame	2096.110	-1284.265	2186.033
Deconv. Flame	947.643	-261.660	1940.388

4 Results & Discussion

4.1 Method-1: Calibration Using Reference Temperatures

Intensity ratio images (G_{850}/G_{925ND}) were calculated for the methane-oxygen flame and the polynomial fit from **Figure 3.12** was used to determine temperature distribution. Specimen for CH₄OX-1-FL case is shown in **Figure 4.1** below. At higher locations near the end of the flame, the noise in deconvoluted images is slightly higher than the LOS images but the temperatures were to be compared with reference at $z=\text{HAB}=15$ mm where the data quality was similar.

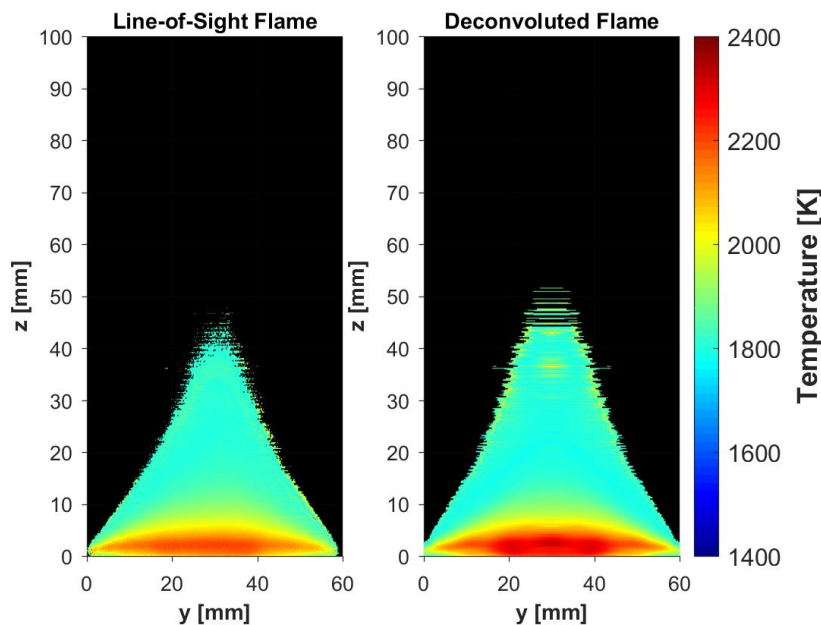


Figure 4.1: Specimen of temperature distribution determined using method-1 for CH₄OX-1-FL

Axial temperature profiles along the centreline were also plotted and compared to the reference values for methane-oxygen flames. An example for the same operating point is shown in **Figure 4.2**. Percentage error from reference temperatures calculated using equation (3.9) are also plotted in the same figure. It can be seen that the errors are high close to the burner surface reaching maximum of 33% at $z=1$ mm. This can be due to the fact that the camera central plane was not perfectly aligned with the burner surface and an overlap in the image was found for a distance of ~ 3 mm from the base. Also, note that in the previous study, reference temperatures close to the burner surface were determined with thermocouple and have lower certainty than temperatures at higher locations which were determined using two-line method.

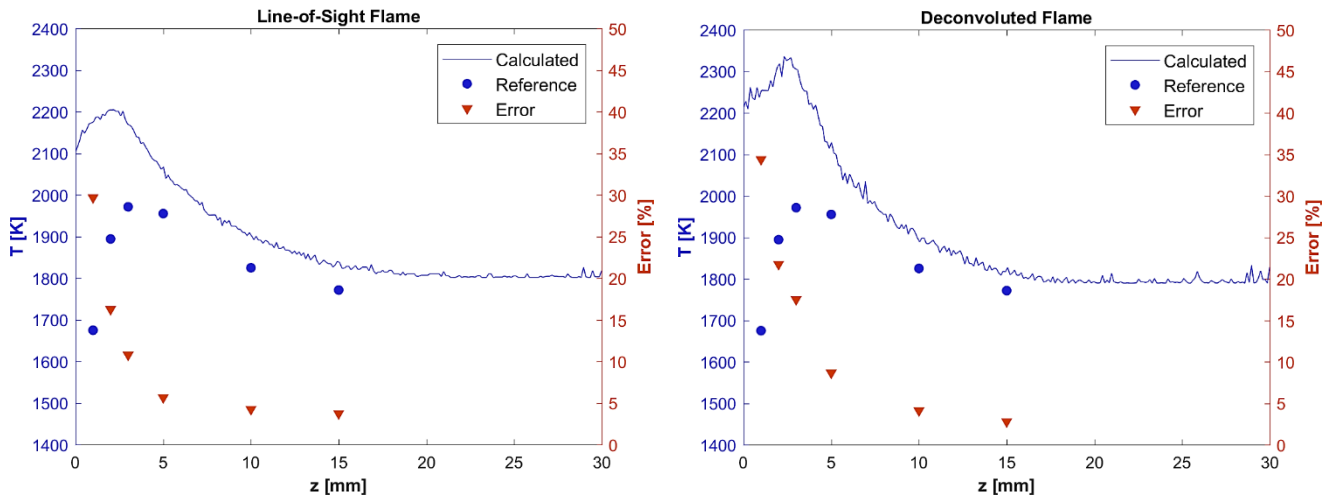


Figure 4.2: Specimen of axial temperature profiles determined using method-1 for CH4OX-1-FL

The error is within 8% at $z \geq 5$ mm and declines with the height. This error can be partly attributed to the error in pressure which was 3% for this case. A lower error in pressure would produce a lower error in the temperature.

4.2 Method-2: Calibration Using TFP

Following the same procedure as in §4.1, intensity ratio images (G_{850}/G_{925ND}) were evaluated and polynomial fit from **Figure 3.14** was used to determine the 2D temperature distribution for methane-oxygen and methane-air flames. An example for CH4OX-1-FL is shown in the **Figure 4.3** below.

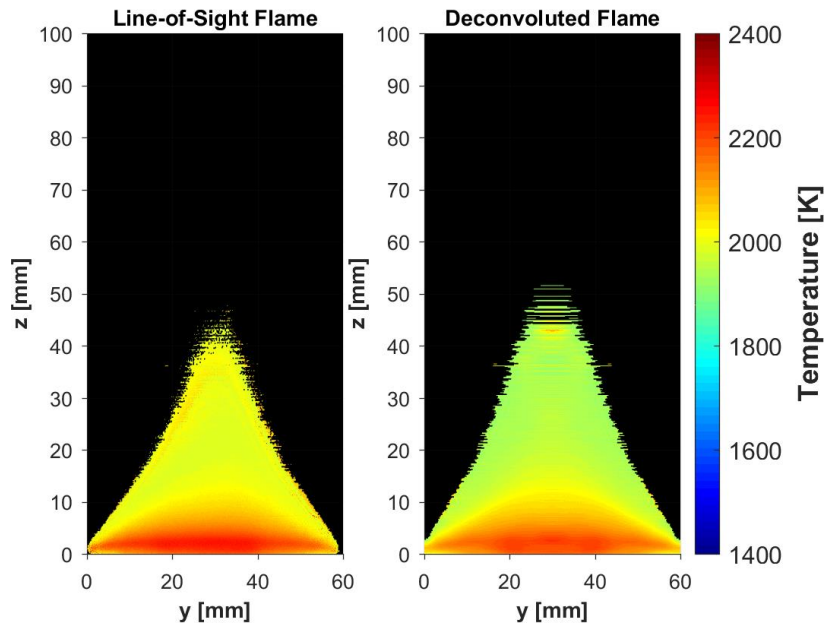


Figure 4.3: Specimen of temperature distribution using method-2 for CH4OX-1-FL

Axial temperature profiles were also plotted and the error in method-2 was evaluated by comparing the calculated temperatures to the known reference temperatures using equation (3.9) as shown in **Figure 4.4**. Again, the temperatures close to the burner surface produced higher errors (maximum of ~30%) and error was much lower above $z=5$ mm (maximum of ~13%) with minimum error of ~10% occurring at $z=5$ mm.

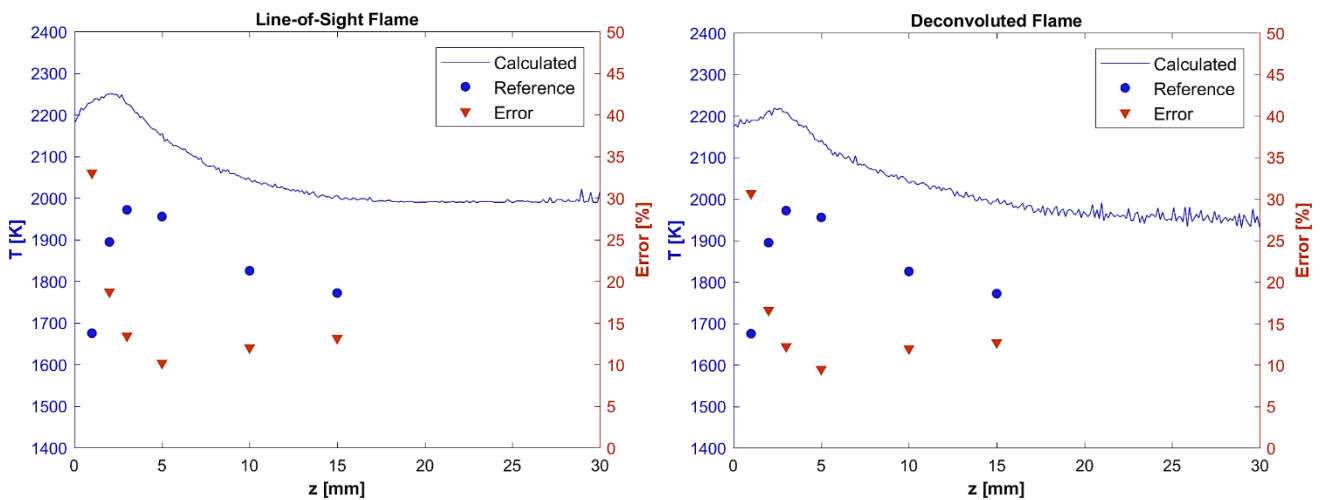


Figure 4.4: Specimen of axial temperature profiles determined using method-2 for CH4OX-1-FL

The same calibration curve and procedure was also applied for evaluating the temperature distribution for methane-air flames, an example is shown in **Figure 4.5**

below. In all methane-air flames, the results were good for up to 80% of the total flame height after which the image noise was high.

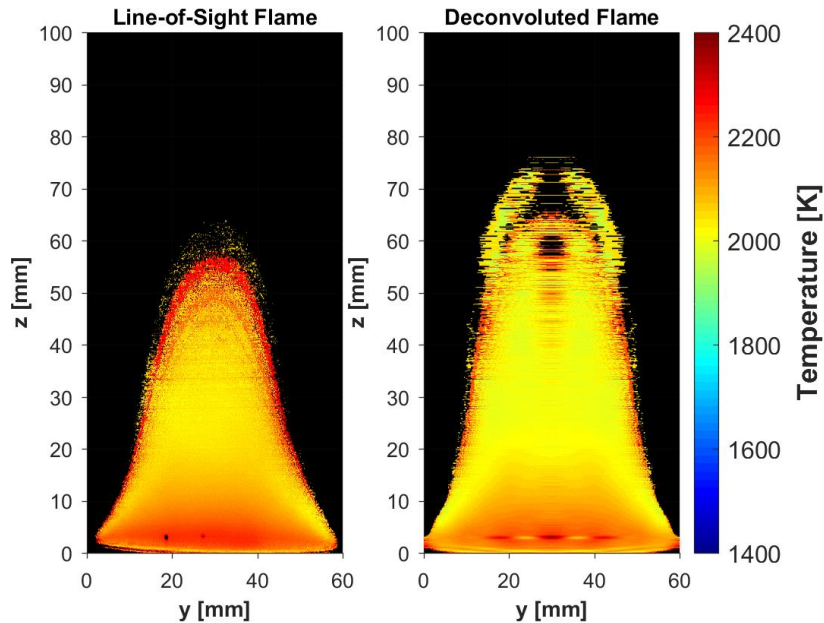


Figure 4.5: Specimen of temperature distribution using method-2 for CH₄AIR-20-FL

Since reference temperatures were known only for HAB=15 mm for methane-air flames, the temperatures were determined by averaging the temperature for a 3 x 3 pixels box centred at this position. **Table 4.1** below summarises the findings along with the average error in pressures. Minimum error of 1.4% was found for case 22 while the maximum error of 7.33% was found for case 6, thus error for methane-air flames was lower than that of methane-oxygen. Although the maximum error in the supply pressures was 10%, it was different for different cases and is translated directly to the errors in temperature. For instance, the average error in pressures for case 22 was 1.7% and therefore the error in temperature is also low, that is 1.4%. This means that the results are reliable. If the pressures/flowrates would have been controlled better, the error in temperatures would have been much smaller. Furthermore, the calibration curve produced using rich methane-oxygen flames produced reasonably good results for methane-air flames in rich (case 20), lean (case 6), and stoichiometric (case 8 & 22) operating conditions.

Table 4.1: Results of method-2 for methane-air flames

Case	HAB [mm]	T _{ref} [K]	LOS Flame		Deconv. Flame	
			T _{calc} [K]	Error [%]	T _{calc} [K]	Error [%]
6	15	1799	1994.40	9.80	1941.20	7.33
8	15	1886	2024.00	6.82	2032.80	7.22
20	15	1929	2074.50	7.01	2060.50	6.38
22	15	2100	2173.20	3.37	2129.80	1.40

4.3 Comparison of Method-1 & Method-2

It is evident that temperatures determined using method-2 are higher than those determined using method-1 while both the methods resulted in temperatures higher than corresponding reference temperatures. In both the methods, temperature errors are mainly due to the error in pressure regulation (and hence flowrates) with some contribution from the inaccuracy of calibration/measurement technique used. Comparing the methane-oxygen flames, method-2 produced a little higher errors than method-1 but of the same order of magnitude as reported in [19]. As an example, a deviation from reference temperature at HAB=5 mm for CH₄OX-1-FL case is 169 K in method-1 and 185 K in method-2, considering the deconvoluted images. This is because method-2 had an additional error contribution associated with TFP measurement. Furthermore, as shown in **Figure 4.2** and **Figure 4.4**, the error gradually increases with height above 5 mm for method-2 in contrast to method-1. The method-2 applied to methane-air flames produced very results with an accuracy comparable to that obtained by applying method-1 to methane-oxygen flames. A maximum temperature deviation of 142 K and a minimum deviation of 30 K was observed for methane-air flames. These are reasonably good results considering the non-scientific grade camera and other low-precision hardware used in the experiments.

Moreover, the errors were in general lower for deconvoluted flame images than for LOS images in both the methods. This is because the reference temperatures known from previous studies were all determined along the central plane and therefore deconvolution was found to be necessary.

5 Application to Rocket Engine

5.1 Differences b/w Current Study & Rocket Engine

The current study used low Reynolds number, premixed methane-air and methane-oxygen flames at atmospheric pressure for developing the calibration curves. Although the SIE-RCC rocket engine uses the same methane-oxygen fuel-oxidiser combination, the flame is different from the current flames in following aspects.

5.1.1 Diffusion Flame

The rocket engine flame is a diffusion flame where rate of reaction is governed by rate of mixing in contrast to premixed flames where burning velocity (function of chemistry) is the governing factor. As a result, the reaction is slower, temperatures are relatively lower, and soot formation is higher particularly at higher distances from the burner exit [55]. The spectral distributions for a premixed and diffusion methane flame are compared in the NIR region in **Figure 5.1** below [56]. Comparison of curves 1 and 2 show that diffusion flames have higher radiation intensity than premixed flames. However, the offset between the two curves varies with wavelength and therefore the ratio between any two bands (e.g. A & C) would not be the same. But if the two bands are narrow (e.g. A & B), located very close to each other, in the 800-950 nm range, the difference in ratio for premixed and diffusion flames would not be large. Thus, the calibration curve developed for premixed flame when applied to diffusion flame would have minor error due to different spectral character but should give reasonable results.

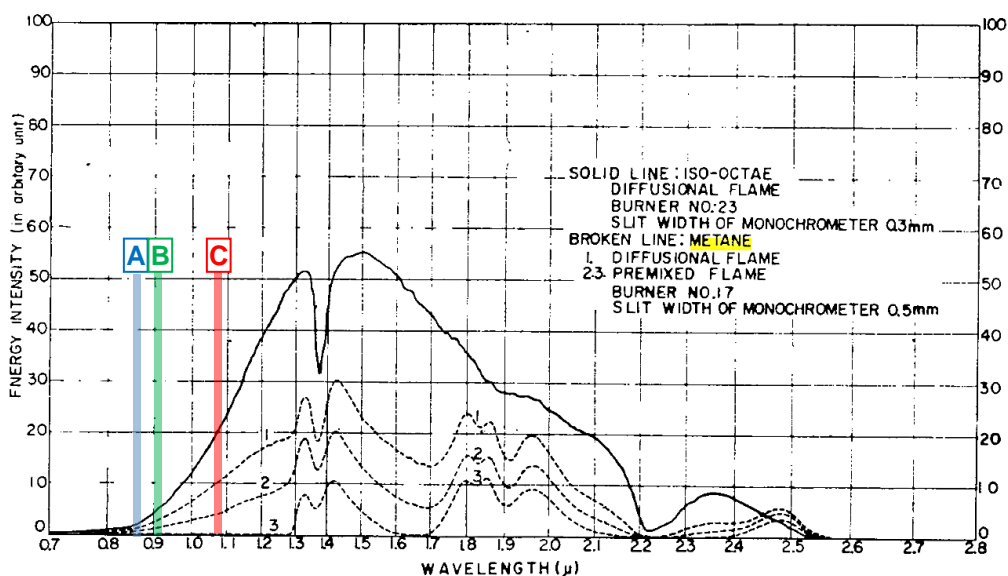


Figure 5.1: Comparison of diffusion & premixed methane flame spectra in NIR region [56]

5.1.2 Confined Flame

The rocket engine flame is confined inside the combustor in contrast to an open-air flame. The combustor walls are capacitively cooled and are at different temperature than the flame. This results in a radiation heat exchange between the flame and the combustor walls. Part of flame radiation is also reflected from the combustor walls. An analysis may be necessary to determine the radiation coming directly from the flame.

5.1.3 High Turbulence

All the reference and measured flames were laminar in nature. Due to smaller dimensions of the burner (~6 mm injector diameter in contrast to 60 mm McKenna disc diameter), the rocket engine flame would have high turbulence. This means higher flickering in the flame which is not problematic since only temporally averaged temperature distribution is of interest. Furthermore, turbulence enhances mixing which decreases the deviation in burning speed (and thus temperature) between the premixed and diffusion flames.

5.1.4 Higher Pressure

The pressure inside the combustor would be 10-20 bar contrary to being atmospheric pressure as in the case for McKenna flames. Increased pressure causes an increase in soot loading resulting in increased radiative emission and possibly lower temperatures (due to higher heat loss through radiation) [57], [58]. Increased pressure also causes pressure/collisional broadening of individual spectral lines [59]. However, it does not affect the measurement since the signals used in band ratio technique are integrated over the bandwidth and are not the values of peak heights. Moreover, any change in the absolute signal values would be equal in the two closely-spaced NIR bands. Thus, the intensity ratios remain unaffected and the same calibration could be used. This has been validated by Nakaya et al. who showed reasonably accurate results for flame thermography in a rapid compression machine by using a calibration curve developed on McKenna burner [19].

5.2 Application of Current Study to Rocket Engine

In the present study, the measurements were evaluated using reference temperatures only within HAB=15 mm. There is very little or no soot present in premixed methane flames close to the burner exit. Therefore, the radiation measured in the selected spectral bands comprised mainly of H₂O emission. However, there will be some soot present for rich conditions even in the premixed flames. It is found that the calibration curve developed gives reasonably good results for rich, lean, and stoichiometric

mixtures particularly for methane-air flames (see **Table 4.1**). This suggests that even if some soot is present, it does not affect the ratio of two spectral bands significantly. However, care must be observed when applying this calibration curve to flames with high soot loading.

Even for premixed methane flames, the soot loading is higher under higher pressures. A shift from premixed to diffusion flame also contributes to increasing soot. However, the optical window in the test rig covers only a distance of 40 mm from the injector exit. A sample image of the rocket engine flame taken using a high speed colour camera is shown in **Figure 5.2** below [44]. Note that the flame is mostly dominated by blue radiation in this region except for the reflection from copper walls. Such emission is characteristic of a non-sooty flame region since soot dominated flame glows yellow. It hints that the flame in optical window region is not overwhelmed by soot.

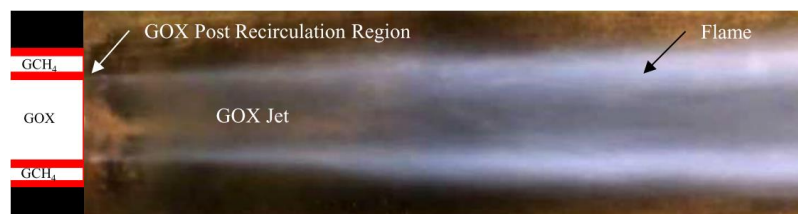


Figure 5.2: Specimen of flame image in rocket engine test rig [44]

Moreover, the emissivity of the commercial copper is very low (~ 0.04 [60]) and therefore the radiation coming out of the window is mostly direct flame radiation and flame radiation reflected from walls. Contribution of radiation emitted by copper walls would be very low.

These considerations collectively suggest that the developed calibration curve can be used for the temperature estimation in the SIE-RCC rocket engine. The effect of quartz window would be cancelled in the ratio since its transmission is almost the same in the two spectral bands. As the calibration has an inherent average error of $\sim 10\%$, the final error in the rocket flame temperature would be similar or little higher. Also, note that the number of operating points for which validation could be performed was limited. The same experiments can be repeated with increased number of operating points and better control of flowrates to increase its reliability. Moreover, further development of the procedure is recommended to quantify the error in procedure's applicability to rocket engine flame.

5.3 Further Development

Though expected to be negligible to small in content within the optical window region, it is advisable to estimate the soot generation in rocket engine flame using a numerical simulation. This will ease in establishing an analytical relation between intensity ratio

and the flame temperature. However, the following approaches can be considered even without simulating the soot loading and without requiring any further experiments. These approaches can also be worked in reverse to estimate the soot content using reference temperatures.

5.3.1 Method-A: Modelling Flame Spectra

The high temperature molecular spectroscopic database (e.g. HITRAN or HITEMP [61], [62]) can be used to develop spectral distribution curves of H₂O emission spectra in NIR range. An example for CO₂, H₂O emission from CH₄-air flame is shown in **Figure 5.3** in which the emission measured for a H₂-air flame using spectrometer is also shown [19]. Contribution from CO₂ is negligible in this NIR region. Although the absolute intensities differ, the relative distribution of modelled and measured spectra are the same. Increasing the temperature not only increases the intensities, but also affect the shape of the curve thus making intensity ratio a function of temperature.

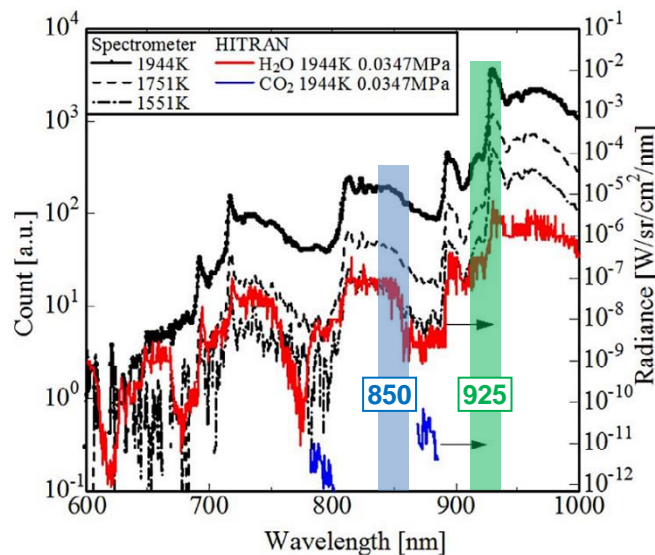


Figure 5.3: Modelled and measured H₂O NIR spectra [19]

The soot, if present, will also contribute to this radiation. Since its radiation is approximated by a temperature dependent Planck's distribution curve, it will increase the sensitivity of the temperature-intensity ratio relation [40]. Emissivity of the soot depends upon temperature and its content (volume fraction) which varies spatially within a flame. Having an idea about its content, a constant emissivity can be assumed for a small region (within optical window) of the entire flame for a simplistic analysis. Then by evaluating the sum of soot and H₂O emission as a function of temperature, a correlation can be found between the intensity ratio of two bands and the temperature. Such approach has been reported by Ellis [41]. This correlation can also be validated using the reference temperatures.

5.3.2 Method-B: Modelling Flame Emissivity

The second approach is to estimate the combined emissivity of H₂O and soot in the selected spectral bands. The gas emissivities are usually a function of temperature, partial pressure (concentration), and path length. Assuming a fairly constant H₂O concentration is reasonable in the flames being discussed [49] and path length can be known by assuming a fixed geometry or can be avoided by using deconvoluted images instead of LOS (latter needs to be further evaluated.) Then the H₂O emissivity would become a function of temperature only and can be determined using either a theoretical model [63] or a correlation for experimental data [64]. A fixed fraction of soot can also be considered and combined emissivity can be determined as a function of temperature only [2], [40], [65]. Using this emissivity function in equation (3.6) will give the flame temperature which can be compared to reference temperatures.

5.3.3 Considerations for Cavity Radiation

Due to very low emissivity of copper-made combustor walls, the interference of wall emission with original flame radiation is expected to be small. However, in order to quantify this error, a cavity analysis as described in [2] can be considered. Moreover, correction for reflection from the copper walls can be performed as mentioned in [66]. Determination of these errors and hence correction in the evaluation would improve the results.

5.3.4 Handling Image Noise

Even a small amount of noise in the single frame image (either 850 nm or 925 nm) causes a serious noise in the intensity ratio image. Therefore, the temperature distributions calculated are also noisy particularly at $z > 60$ mm. This noise can be reduced by performing smoothing/filtering operation either on the individual frames or the intensity ratio image. The image filtering is a convolution operation in which the intensity at a given pixel is calculated from its neighbours using mean, median, exponential weighting etc. The type of filter and the frame(s) to which it should be applied would have to be determined by evaluating the results with different combinations.



6 Conclusion

A fairly simple optical method of measuring temporally averaged, spatially resolved 2D flame temperature fields was developed based on band ratio technique. A calibration of temperature against intensity ratio was performed either using reference temperatures or a TFP. In both the calibration methods, inaccuracy in supply pressures was the main source of error. However due to inhomogeneity in the TFP fibre, former method was slightly more accurate than the latter. The same calibration gives reasonably good results when applied to both, methane-air and methane-oxygen flames in lean, rich, and stoichiometric cases. The errors were higher for line-of-sight images than for deconvoluted images which was expected since all the reference temperatures were known along the central plane. In latter case, error ranged from a minimum of 1.4% to a maximum of 27% while being within 10% in most of the cases. The reliability of the procedure can be increased by repeating the experiments with increased number of operating points and better control of supply pressures. Possibilities of further investigating the same data without any additional experiments are also discussed.

References

- [1] P. R. N. Childs, J. R. Greenwood, and C. A. Long, 'Review of temperature measurement', *Review of Scientific Instruments*, vol. 71, no. 8, pp. 2959–2978, Aug. 2000.
- [2] L. S. Marks, *Marks' standard handbook for mechanical engineers*, 11th ed. New York: McGraw-Hill, 2007.
- [3] F. Edler, 'Precise temperature measurement above 1000 °C using thermocouples', p. 10.
- [4] D. Bradley and K. J. Matthews, 'Measurement of high gas temperatures with fine wire thermocouples', *Journal of Mechanical Engineering Science*, vol. 10, no. 4, pp. 299–305, Oct. 1968.
- [5] V. A. Cundy, J. S. Morse, and D. W. Sensor, 'Constant-tension thermocouple rake suitable for use in flame mode combustion studies', *Review of Scientific Instruments*, vol. 57, no. 6, pp. 1209–1210, Jun. 1986.
- [6] B. Ma, G. Wang, G. Magnotti, R. S. Barlow, and M. B. Long, 'Intensity-ratio and color-ratio thin-filament pyrometry: Uncertainties and accuracy', *Combustion and Flame*, vol. 161, no. 4, pp. 908–916, Apr. 2014.
- [7] C. S. Mcenally, M. O. Koylu, and L. D. Pfefferle, 'Soot Volume Fraction and Temperature Measurements in Laminar Nonpremixed Flames Using Thermocouples', p. 20.
- [8] A. Moallemi, 'Experimental investigation of the effect of NaCl additive on the formation and evolution of particles in a diffusion flame', MSc, University of Alberta, 2017.
- [9] R. Ghoddoussi, 'An investigation on thermal characteristics of premixed counterflow flames using micro- thermocouples', MSc, University of Maryland, 2005.
- [10] M. V. Heitor and A. L. N. Moreira, 'Thermocouples and sample probes for combustion studies', *Progress in Energy and Combustion Science*, vol. 19, no. 3, pp. 259–278, Jan. 1993.
- [11] A. Ballantyne and J. B. Moss, 'Fine wire thermocouple measurements of fluctuating temperature', *Combustion Science and Technology*, vol. 17, no. 1–2, pp. 63–72, Oct. 1977.
- [12] A. Yule, D. Taylor, and N. Chigier, 'On-line digital compensation and processing of thermocouple signals for temperature measurement in turbulent flames', in *16th Aerospace Sciences Meeting*, Huntsville, AL, U.S.A., 1978.
- [13] V. Vilimpoc and L. P. Goss, 'SiC-Based thin-filament pyrometry: Theory and thermal properties', *Symposium (International) on Combustion*, vol. 22, no. 1, pp. 1907–1914, Jan. 1989.

- [14] J. D. Maun, P. B. Sunderland, and D. L. Urban, 'Thin-filament pyrometry with a digital still camera', *Applied Optics*, vol. 46, no. 4, p. 483, Feb. 2007.
- [15] P. Struk, D. Dietrich, R. Valentine, and I. Feier, 'Comparisons of gas-phase temperature measurements in a flame using thin-filament pyrometry and thermocouples', in *41st Aerospace Sciences Meeting and Exhibit*, Reno, Nevada, 2003.
- [16] D. Blunck, S. Basu, Y. Zheng, V. Katta, and J. Gore, 'Simultaneous water vapor concentration and temperature measurements in unsteady hydrogen flames', *Proceedings of the Combustion Institute*, vol. 32, no. 2, pp. 2527–2534, 2009.
- [17] P. B. Kuhn, B. Ma, B. C. Connelly, M. D. Smooke, and M. B. Long, 'Soot and thin-filament pyrometry using a color digital camera', *Proceedings of the Combustion Institute*, vol. 33, no. 1, pp. 743–750, 2011.
- [18] L. G. Blevins, M. W. Renfro, K. H. Lyle, N. M. Laurendeau, and J. P. Gore, 'Experimental study of temperature and CH radical location in partially premixed CH₄/air coflow flames', *Combustion and Flame*, vol. 118, no. 4, pp. 684–696, Sep. 1999.
- [19] S. Nakaya, T. Funahashi, Y. Asakami, I. Fujio, S. Takahashi, and M. Tsue, 'Thermometry of combustion gas measuring two-band near-infrared emissions less than 1.1 μm from water molecules', *Experimental Thermal and Fluid Science*, vol. 94, pp. 1–8, Jun. 2018.
- [20] P. J. Dyne, 'Optical methods for the determination of combustion temperatures', *Journal of the American Rocket Society*, vol. 23, no. 3, pp. 165–169, May 1953.
- [21] H. Zhao and N. Ladommatos, 'Optical diagnostics for soot and temperature measurement in diesel engines', *Progress in Energy and Combustion Science*, vol. 24, no. 3, pp. 221–255, Jan. 1998.
- [22] P. R. N. Childs, *Practical temperature measurement*. Oxford: Butterworth-Heinemann, 2001.
- [23] B. Ma and M. B. Long, 'Absolute light calibration using S-type thermocouples', *Proceedings of the Combustion Institute*, vol. 34, no. 2, pp. 3531–3539, Jan. 2013.
- [24] C. de Izarra and J.-M. Gitton, 'Calibration and temperature profile of a tungsten filament lamp', *European Journal of Physics*, vol. 31, no. 4, pp. 933–942, Jul. 2010.
- [25] B. Nie, X. He, C. Zhang, X. Li, and H. Li, 'Temperature measurement of gas explosion flame based on the radiation thermometry', *International Journal of Thermal Sciences*, vol. 78, pp. 132–144, Apr. 2014.
- [26] E. Planas-Cuchi, J. M. Chatris, C. López, and J. Arnaldos, 'Determination of flame emissivity in hydrocarbon pool fires using infrared thermography', *Fire Technology*, vol. 39, no. 3, pp. 261–273, Jul. 2003.

- [27] V. J. Lyons and C. M. Gracia-Salcedo, 'Determination of combustion gas temperatures by infrared radiometry in sooting and nonsooting flames', *NASA*, no. 88-C-008, p. 14, 1989.
- [28] A. Àgueda, E. Pastor, Y. Pérez, and E. Planas, 'Experimental study of the emissivity of flames resulting from the combustion of forest fuels', *International Journal of Thermal Sciences*, vol. 49, no. 3, pp. 543–554, Mar. 2010.
- [29] T. Astarita and G. M. Carlomagno, *Infrared thermography for thermo-fluid-dynamics*. Berlin, Heidelberg: Springer Berlin Heidelberg, 2013.
- [30] M. Vollmer and K.-P. Möllmann, *Infrared thermal imaging: Fundamentals, research and applications*, Second edition. Weinheim, Germany: Wiley-VCH Verlag GmbH & Co. KGaA, 2018.
- [31] FLIR, *The ultimate infrared handbook for R&D professionals*. USA: FLIR, 2012.
- [32] T.-W. Lee, *Thermal and flow measurements*. Boca Raton: CRC Press, 2008.
- [33] Y. Huang and Y. Yan, 'Transient two-dimensional temperature measurement of open flames by dual-spectral image analysis', *Transactions of the Institute of Measurement and Control*, vol. 22,5, pp. 371–384.
- [34] Gang Lu, Yong Yan, G. Riley, and H. C. Bheemul, 'Concurrent measurement of temperature and soot concentration of pulverized coal flames', *IEEE Transactions on Instrumentation and Measurement*, vol. 51, no. 5, pp. 990–995, Oct. 2002.
- [35] J. V. Pastor, J. M. García-Oliver, A. García, C. Micó, and S. Möller, 'Application of optical diagnostics to the quantification of soot in n-alkane flames under diesel conditions', *Combustion and Flame*, vol. 164, pp. 212–223, Feb. 2016.
- [36] H. C. Hottel and F. P. Broughton, 'Determination of true temperature and total radiation from luminous gas flames', *Industrial & Engineering Chemistry Analytical Edition*, vol. 4, no. 2, pp. 166–175, Apr. 1932.
- [37] T. S. Draper, D. Zeltner, D. R. Tree, Y. Xue, and R. Tsiava, 'Two-dimensional flame temperature and emissivity measurements of pulverized oxy-coal flames', *Applied Energy*, vol. 95, pp. 38–44, Jul. 2012.
- [38] G. Lu and Y. Yan, 'Temperature profiling of pulverized coal flames using multicolor pyrometric and digital imaging techniques', *IEEE Transactions on Instrumentation and Measurement*, vol. 55, no. 4, pp. 1303–1308, Aug. 2006.
- [39] W. Eckl, V. Weiser, and N. Eisenreich, 'Spectroscopic flame diagnostics by analyzing NIR water bands', *The Fifth International Symposium On Special Topics In Chemical Propulsion: Combustion of Energetic Materials*, 2000.
- [40] C. C. Ferriso, C. B. Ludwig, and F. P. Boynton, 'A band-ratio technique for determining temperatures and concentrations of hot combustion gases from infrared-emission spectra', *Symposium (International) on Combustion*, vol. 10, no. 1, pp. 161–175, Jan. 1965.

- [41] D. J. Ellis, V. P. Solovjov, and D. R. Tree, 'Temperature measurement using infrared spectral band emissions from water', MSc, Brigham Young University - Provo, 2016.
- [42] M. Lyonnet, B. Deleglise, and G. Grenat, 'The two-component PSP investigation on a civil aircraft model in S2MA wind tunnel', *AGARD CP-601*, 1997.
- [43] V. P. Kulesh, A. N. Morozov, V. E. Mosharov, and V. N. Radchenko, 'Application of a Prism Image Splitter for Pressure Distribution Measurements Using Two-Color Luminescent Sensors', vol. 44, no. 1, p. 4, 2001.
- [44] F. F. Winter, S. Silvestri, M. P. Celano, G. Schlieben, and O. J. Haidn, 'High-speed & emission imaging of a coaxial single element GOX/GCH₄ rocket combustion chamber', *7th European conference for aeronautics and space sciences (eucass)*, p. 10, 2017.
- [45] 'McKenna Burner', www.flatflame.com. [Online]. Available: <http://flatflame.com/burner-description.html>. [Accessed: 13-Feb-2019].
- [46] S. Prucker, W. Meier, and W. Stricker, 'A flat flame burner as calibration source for combustion research: Temperatures and species concentrations of premixed H₂/air flames', *Review of Scientific Instruments*, vol. 65, no. 9, pp. 2908–2911, Sep. 1994.
- [47] 'CeraFib GmbH - hochtemperaturbeständige keramische Filamente, Werkstoffe und Bauteile'. [Online]. Available: <http://www.cerafib.de/>. [Accessed: 15-Feb-2019].
- [48] P. Weigand, R. Lückcrath, and W. Meier, 'Documentation of flat premixed laminar CH₄/air standard flames: Temperatures & species concentrations', Jan. 2003.
- [49] F. Xu, K.-C. Lin, and G. M. Faeth, 'Soot formation in laminar premixed methane/oxygen flames at atmospheric pressure', *Combustion and Flame*, vol. 115, no. 1–2, pp. 195–209, Oct. 1998.
- [50] A. D'Amato, 'Development of an abel transform algorithm for combustion characterization and data analysis', Master's Thesis, Technische Universität München; Politecnico Di Torino, Germany; Italy.
- [51] F. Payri, J. V. Pastor, J. M. García, and J. M. Pastor, 'Contribution to the application of two-colour imaging to diesel combustion', *Measurement Science and Technology*, vol. 18, no. 8, pp. 2579–2598, Aug. 2007.
- [52] C. E. Baukal, *Oxygen-enhanced combustion*. Boca Raton: CRC Press, 2013.
- [53] W. M. Rohsenow, J. P. Hartnett, and Y. I. Cho, Eds., *Handbook of heat transfer*, 3rd ed. New York: McGraw-Hill, 1998.
- [54] D. Williams and M. Curry, 'Prediction of Rigid Silica Based Insulation Conductivity', *NASA*, p. 144, 1993.
- [55] A. G. Gaydon, *The spectroscopy of flames*, 2nd ed. Dordrecht: Springer-Science + Business media, 1974.

- [56] R. Echigo, N. Nishiwaki, and M. Hirata, 'A study on the radiation of luminous flames', p. 9.
- [57] S. J. Brookes and J. B. Moss, 'Measurements of soot production and thermal radiation from confined turbulent jet diffusion flames of methane', *Combustion and Flame*, vol. 116, no. 1–2, pp. 49–61, Jan. 1999.
- [58] H. Gohari Darabkhani and Y. Zhang, 'Pressure Effects on Structure and Temperature Field of Laminar Diffusion Flames', in *48th AIAA Aerospace Sciences Meeting Including the New Horizons Forum and Aerospace Exposition*, Orlando, Florida, 2010.
- [59] C. B. Ludwig, W. Malkmus, J. E. Reardon, J. A. L. Thomson, and R. Goulard, *Handbook of infrared radiation from combustion gases NASA SP-3080*, vol. 3080. NASA, 1973.
- [60] T. L. Bergman and F. P. Incropera, Eds., *Fundamentals of heat & mass transfer*, 7th ed. Hoboken, NJ: Wiley, 2011.
- [61] I. E. Gordon *et al.*, 'The HITRAN2016 molecular spectroscopic database', *Journal of Quantitative Spectroscopy and Radiative Transfer*, vol. 203, pp. 3–69, Dec. 2017.
- [62] L. S. Rothman *et al.*, 'HITEMP, the high-temperature molecular spectroscopic database', *Journal of Quantitative Spectroscopy and Radiative Transfer*, vol. 111, no. 15, pp. 2139–2150, Oct. 2010.
- [63] K. Andersson and F. Johnsson, 'Flame and radiation characteristics of gas-fired O₂/CO₂ combustion', *Fuel*, vol. 86, no. 5–6, pp. 656–668, Mar. 2007.
- [64] A. K. Mehrotra, K. Karan, and L. A. Behie, 'Estimate gas emissivities for equipment and process design', *Chemical Engineering Progress*, p. 8, 1995.
- [65] J. D. Felske and C. L. Tien, 'Calculation of the emissivity of luminous flames', *Combustion Science and Technology*, vol. 7, no. 1, pp. 25–31, Mar. 1973.
- [66] Z. Yang, A. Adeosun, B. M. Kumfer, and R. L. Axelbaum, 'An approach to estimating flame radiation in combustion chambers containing suspended-particles', *Fuel*, vol. 199, pp. 420–429, Jul. 2017.

Annexures

A.1 MATLAB Script for Method-1

Calibration using methane-air data and validation using methane-oxygen data.

%% Start

```
clc; clear;
```

%% Read Images

```
% Non-Normalised Image Pairs
g1=im2double(imread('mean850_587_rot_crop.bmp'));
g2=im2double(imread('mean925_587_rot_crop.bmp'));

% Normalised Deconvoluted Image Pairs
g1dec=im2double(imread('mean850_587_rot_crop_deconNorm.bmp'));
g2dec=im2double(imread('mean925_587_rot_crop_deconNorm.bmp'));
```

%% Calculate Intensity Ratios

```
ratio=g1./g2;
ratio(isinf(ratio))=0;
ratio(isnan(ratio))=0;
ratio(ratio>=1)=0;

ratioDec=g1dec./g2dec;
ratioDec(isinf(ratioDec))=0;
ratioDec(isnan(ratioDec))=0;
ratioDec(ratioDec>=1)=0;
```

%% Calibration Curve

```
% Polynomial Fit Coefficients for Flame
h=[2749.190932 -1520.428432 2011.917671];
for i=1:size(g1,1)
    for j=1:size(g1,2)
        t(i,j)=polyval(h,ratio(i,j));
    end
end
t(t==polyval(h,0))=NaN;
% Polynomial Fit equation for Deconvoluted Flame
hD=[4023.830538 -2646.506294 2224.516972];
for i=1:size(g1,1)
    for j=1:size(g1,2)
        tD(i,j)=polyval(hD,ratioDec(i,j));
    end
end
tD(tD==polyval(hD,0))=NaN;
```

%% Plots of Temperature Distribution Images

```
za=linspace(0,100,size(g1,2));
ya=linspace(0,60,size(g1,1));
[Z,Y]= meshgrid(za,ya);
figure(1)
ax(1)=subplot(1,2,1)
surf(Y,Z,t)
xlabel('y [mm]','fontWeight','bold')
ylabel('z [mm]','fontWeight','bold')
title('Line-of-Sight Flame')
shading interp
axis([0 60 0 100])
caxis([1400 2400])
colormap(jet)
set(gca,'color','black','TickDir','out')
ax(2)=subplot(1,2,2)
surf(Y,Z,tD)
xlabel('y [mm]','fontWeight','bold')
ylabel('z [mm]','fontWeight','bold')
title('Deconvoluted Flame')
shading interp
axis ([0 60 0 100])
caxis([1400 2400])
colormap(jet)
set(gca,'color','black','TickDir','out')
h=colorbar;
set(h,'Position',[0.8314 0.11 0.0281 0.8150],'fontSize',12)
ylabel(h,'Temperature [K]','fontWeight','bold','fontSize',14)
for i=1:2
    pos=get(ax(i),'Position');
    set(ax(i),'Position',[0.9*pos(1) pos(2) 0.9*pos(3) pos(4)]);
end
set(gcf,'color','white');
% export_fig method_B_Temp_Images.png -m2;
```

%% Evaluate Ratios, Temperatures, Errors at Specific Axial Positions

```
sc=101/13; % Image scale in pixels/mm (101/13 met-ox, 121/15 met-air)
n=3; % Averaging size n x n pixels
z=[5 10 15 19.8736 24.922]; % Axial locations to process in mm
zz=round(z.*sc);
% Reference temperatures
tRef=[1955.108557 1824.790176 1771.417003 1677.63 1633.52];
yc=ceil(size(g1,1)/2);
y1=yc-floor(n/2);
y2=yc+floor(n/2);

ratioResult=[];
ratioResultDec=[];
tRes=[];
tDecRes=[];
error=[];
errorDec=[];

for i=1:length(zz)
    zc=zz(i);
    z1=zc-floor(n/2);
    z2=zc+floor(n/2);
    ratioM=ratio(y1:y2,z1:z2);
    ratioM=mean(mean(ratioM));
    ratioResult=[ratioResult ratioM];
    ratioMDec=ratioDec(y1:y2,z1:z2);
```

```
ratioMDec=mean(mean(ratioMDec));  
ratioResultDec=[ratioResultDec ratioMDec];  
tM=t(y1:y2,z1:z2);  
tM=mean(mean(tM));  
tRes=[tRes tM];  
err=100*abs(tRef(i)-tM)/tRef(i);  
error=[error err];  
tDecM=tD(y1:y2,z1:z2);  
tDecM=mean(mean(tDecM));  
tDecRes=[tDecRes tDecM];  
errDec=100*abs(tRef(i)-tDecM)/tRef(i);  
errorDec=[errorDec errDec];  
  
end
```

%% Plots of Axial Temperature Profiles

```
tz=t(ceil(size(g1,1)/2),:);  
tzD=tD(ceil(size(g1,1)/2),:);  
% Line-of-Sight Flame  
fig2=figure(2)  
left_color=[0.1 0.1 0.8];  
right_color=[0.8 0.2 0.0];  
set(fig2,'defaultAxesColorOrder',[left_color; right_color]);  
set(gcf,'color','white');  
yyaxis left  
plot(z,tz)  
hold on  
ylabel('T [K]','fontweight','bold')  
axis ([0 30 1400 2400])  
scatter(z,tRef,'filled','o','linewidth',2)  
hold on  
yyaxis right  
ylabel('Error [%]','fontweight','bold')  
axis ([0 30 0 40])  
scatter(z,error,'filled','v')  
legend({'Calculated','Reference','Error'},'FontSize',11)  
title('Line-of-Sight Flame')  
xlabel('z [mm]','fontweight','bold')  
% Deconvoluted Flame  
fig3=figure(3)  
left_color=[0.1 0.1 0.8];  
right_color=[0.8 0.2 0.0];  
set(fig3,'defaultAxesColorOrder',[left_color; right_color]);  
set(gcf,'color','white');  
yyaxis left  
plot(z,tzD)  
hold on  
ylabel('T [K]','fontweight','bold')  
axis ([0 30 1400 2400])  
scatter(z,tRef,'filled','o','linewidth',2)  
hold on  
yyaxis right  
ylabel('Error [%]','fontweight','bold')  
axis ([0 30 0 40])  
scatter(z,errorDec,'filled','v')  
legend({'Calculated','Reference','Error'},'FontSize',11)  
title('Deconvoluted Flame')  
xlabel('z [mm]','fontweight','bold')  
  
% clearvars -except ratioResult ratioResultDec;
```

A.2 MATLAB Script for Method-2

Use fibre temperature to calibrate methane-oxygen intensity ratios. Use calibration curve to estimate temperatures for methane-oxygen & methane-air flames. Compare estimated temperatures with reference data.

%% Start

```
clc; clear;
```

%% Read Images

```
% Read Non-Normalised Image Pairs of Flame
g1=im2double(imread('mean850_160_rot_crop.bmp')); % 850 Exp-1
g2=im2double(imread('mean925_160_rot_crop.bmp')); % 925 Exp-1+ND

% Read Non-Normalised Image Pairs of Fiber
f1=im2double(imread('mean850_1001_rot_crop.bmp')); % 850 Exp-2
f2=im2double(imread('mean925_1001_rot_crop.bmp')); % 925 Exp-2

% Scale & Number of Pixels to Process
sc=101/13; % Image scale (pixels/mm) from scaling image (101/13 met-ox, 121/15 met-air)
n=3; % Averaging size n x n pixels
```

%% Normalisation of Exposure Levels

```
zp=30; % Reference Location in px
zpm=round(zp.*sc);
yc=ceil(size(g1,1)/2);
y1=yc-floor(n/2);
y2=yc+floor(n/2);
z1p=zp-floor(n/2);
z2p=zp+floor(n/2);
pMg1=mean(mean(g1(y1:y2,z1p:z2p)));
pMg2=mean(mean(g2(y1:y2,z1p:z2p)));
pMf1=mean(mean(f1(y1:y2,z1p:z2p)));
pMf2=mean(mean(f2(y1:y2,z1p:z2p)));
g1=g1.*(pMf1/pMg1);
g2=g2.*(pMf2/pMg2);
```

%% Remove Flame from Fibre Images

```
f1=f1-g1;
f1(f1<0)=0;
f2=f2-g2;
f2(f2<0)=0;
```

%% Calculate Ratio

```
ratio=f1./f2;
ratio(isinf(ratio))=0;
ratio(isnan(ratio))=0;
```



%% Pixel Locations to Process

```
z=[5];          % Axial locations to process in mm
z=round(z.*sc)
imtool(ratio);
prompt=sprintf('Axial pixel location @ lateral centre of %d =',yc);
zz=input(prompt); % Specify fibre centre in px using imtool
ratioResf=[];

for i=1:length(zz)
    zc=zz(i);
    z1=zc-floor(n/2);
    z2=zc+floor(n/2);
    ratioM=ratio(y1:y2,z1:z2);
    ratioM=mean(mean(ratioM));
    ratioResf=[ratioResf ratioM];
end

ratioResf
```

%% Calculate Temperatures at Specific Locations

```
% Constants
c1=3.74e-16;
c2=1.44e-2;
% Wavelengths
lam1=850e-9;
lam2=925e-9;
% Spectral Response Ratio 850/925=1.856302, 850/925ND=7.889870
sr=1.856302;

% Fiber Temperature (K)
Tf=(c2*(1/lam2-1/lam1))/(log(ratioResf)+log(1/sr)+5*log(lam1/lam2))

% Comparison of Wiens Approximation to Planck's Equation
% T=1905.34 % (e.g. CH40X_01-1.15-FB2)
% ratioRes
% ratioVer=1.856302*((lam2/lam1)^5)*((exp(c2/(lam2*T))-1)/(exp(c2/(lam1*T))-1))
% ratioRes=1.3777, T=1905.3
% ratioVer=1.3774, T=1905.3
% ratioVer=1.3777, T=1905.34 (% error 0.0021)
```

%% Plots of Temperature Distribution Image

```
% Same as in method-1
```

%% Plots of Axial Temperature Profiles

```
% Same as in method-1
```